Title: p73 controls cell junction dynamics during sprouting angiogenesis and acts via Angiomotin

Condensed title: p73 regulates endothelial junctions via AMOT

Laura Maeso-Alonso[1], Hugo Alonso-Olivares[1], Nicole Martínez-García[2], Javier Villoch-Fernández[1], Laura Puente-Santamaría[3], Natalia Colas-Algora[4], Alfonso Fernández-Corona[5], María Elena Lorenzo-Marcos[5], Benilde Jiménez[3,6], Lars Holmgren[7], Margareta Wilhelm[8], Jaime Millan[4], Luis del Peso[3,6], Lena Claesson-Welsh[9], Margarita M. Marques[10], Maria C. Marin[1/*]

[1]Instituto de Biomedicina y Departamento de Biología Molecular, Universidad de León (Spain)

[2]Instituto de Biomedicina y Departamento de Producción Animal, Universidad de León (Spain)

[3]Departamento de Bioquímica, Universidad Autónoma de Madrid (UAM), Instituto de Investigaciones Biomédicas "Alberto Sols" CSIC-UAM, Madrid (Spain)

[4]Centro de Biología Molecular "Severo Ochoa" (CSIC-UAM), Madrid (Spain).

[5]Complejo Asistencial Universitario de León, León (Spain)

[6]IdiPaz, Instituto de Investigación Sanitaria del Hospital Universitario La Paz, Madrid (Spain)

[7]Department of Oncology-Pathology, Bioclinicum, Karolinska Institutet, Stockholm 17164 (Sweden)

[8]Department of Microbiology, Tumor and Cell Biology, Karolinska Institutet, 171 65 Stockholm (Sweden)

[9]Department of Immunology, Genetics and Pathology, Rudbeck Laboratory, Science for Life Laboratory Uppsala University, Uppsala (Sweden).

[10]Instituto de Desarrollo Ganadero y Sanidad Animal y Departamento de Producción Animal, Universidad de León (Spain)

*****Corresponding author: mmarv@unileon.es; ORCID: 0000-0002-7149-287X; Departamento de Biología Molecular, Universidad de León, Campus de Vegazana sn, 24071 León (Spain)

Author Contributions: Conceptualization: L.M.-A., M.M.M. and M.C.M.; investigation: L.M.-A., H.A.-O., N.M.-G., J.V.-F., L.P.-S., N.C.-A.; methodology: L.M.-A., J.V.-F., L.P.-S., J.M., L. d-P., L.C.-W., M.M.M. and M.C.M.; software: L.M.-A.,

H.A.-O., L.P.-S., validation: L.M.-A., J.M., L. d-P., M.M.M. and M.C.M.; formal analysis: L.M.-A., L. d-P., M.M.M. and M.C.M.; visualization: L.M.-A., H.A.-O., N.M.-G., M.M.M. and M.C.M.; writing the original draft, review and editing: L.M.-A., H.A.-O., M.M.M. and M.C.M.; general review and editing: All authors; supervision: L.M.-A., M.M.M. and M.C.M.; resources: A.F.-C., M.E.L.-M, B.J., L.H., M.W., J.M., L. d-P., L.C.-W., M.M.M. and M.C.M.; funding acquisition: M.C.M.; project administration: M.M.M. and M.C.M. All authors have read and agreed to the published version of the manuscript.

Summary: We explore p73 role in vascular morphogenesis and uncover that it orchestrates gene regulation to organize and stabilize the endothelial barrier during sprouting angiogenesis. Mechanistically, TAp73 isoform modulates transcriptional programs involved in vascular architecture including endothelial junction dynamics via AMOT.

Abstract

Vascular development comprises vasculogenesis, sprouting and non-sprouting angiogenesis and vessel assembly and remodeling. These processes require the coordinated regulation of intercellular junctions to maintain vascular architecture and vessel barrier. Here we demonstrate a key function for p73 transcription factor orchestrating transcriptional programs involved in the regulation of endothelial cell junction morphology during sprouting angiogenesis. *TP73* is required for vessel integrity and stability to maintain the endothelial barrier. p73-downregulation leads to hyperpermeability *in vitro*, while total-p73 or TAp73-specific knockout results in hemorrhages *in vivo*. We identified AMOT as a p73 direct transcriptional target. Lack of p73 affects expression, localization, and function of Angiomotin. In turn, stabilization of Angiomotin levels in p73-deficent cells can rescue their junctional defects, altogether demonstrating that AMOT is one of p73-downstream mediators during the regulation of endothelial junction dynamics. These results redefine p73 role in angiogenesis by revealing p73 as a vascular architect that regulates endothelial cell junctions, thereby organizing and stabilizing the endothelial barrier.

Introduction

The formation of the vascular system is one of the earliest events during organogenesis (Heinke *et al*., 2012). This process needs to be spatially and temporally coordinated to ensure proper tissular architecture and endothelium functionality (Duran *et al*., 2017). The formation of *de novo* vessels or vasculogenesis, takes place during embryonic development, but most endothelial cells (EC) retain the capacity to sense and respond to angiogenic signals to generate new vessels from the preexisting ones in a process named angiogenesis (Folkman, 1971). During sprouting angiogenesis, rearrangements of tip and stalk cells require dynamic remodeling of cell-cell junctions while maintaining the integrity of the new sprout to avoid leakage and alteration of vessel homeostasis (Szymborska and Gerhardt, 2018). In this context, endothelial junctions may play a coordinating role, polarizing the activity of the migration machinery and maintaining the sprout cohesion (Szymborska and Gerhardt, 2018). Loss of these junctions promotes hemorrhages and edemas and also plays an important role during tumor angiogenesis (Komarova *et al*., 2017). It has been proposed that junction-associated proteins, like the angiomotin family members AMOT (Angiomotin) and AMOTL1 (Angiomotin-like-1), are involved in the regulation and coordination of front–rear polarity, collective EC migration and junction stability during sprouting angiogenesis (Aase *et al*., 2007, Bratt *et al*., 2005, Ernkvist *et al*., 2009, Zheng *et al*., 2009). However, the upstream regulators of these proteins remain elusive.

In this regard, the *TP73* gene has been described as an essential player during vascular morphogenesis and angiogenesis (Dulloo *et al*., 2015b, Fernandez-Alonso *et al*., 2015, Stantic *et al*., 2015). *TP73* can give rise to different functional isoforms: TAp73 with full transactivation activity, and the truncated dominant-negative DNp73 (Vikhreva *et al*., 2018). The compiled data support the idea that DNp73 functions as a pro-angiogenic signaling factor in tumor cells (Dulloo *et al*., 2015a, Fernandez-Alonso *et al*., 2015, Stantic *et al*., 2015). On the other hand, a bi-functional role in tumor angiogenesis has been proposed for TAp73 (Amelio *et al*., 2015, Dulloo *et al*., 2015b, Stantic *et al*., 2015). However, the physiological function of TAp73 during developmental vascular morphogenesis still needs to be addressed. The *Trp73-/-* mice, which lack both isoforms, exhibit extensive gastrointestinal and cranial hemorrhages (Yang *et al*., 2000), which is suggestive of vascular fragility and/or other defects in their vascular compartment. p73 deficiency also leads to perturbed vascular development in the mouse retina, with accumulation of EC tufts, decrease in vascular branching and elongation, and anastomosis

defects (Fernandez-Alonso *et al*., 2015). Interestingly, similar defects have previously been associated with altered stability or dynamics of EC junctions (Bentley *et al*., 2014, Dejana *et al*., 2008, Giannotta *et al*., 2013, Lenard *et al*., 2013, Sauteur *et al*., 2014). However, whether downregulated levels of TAp73 in EC lead to junctional defects, *in vivo* and/or *in vitro*, and the possible consequences for vascular morphogenesis remain an important open question.

In this work, we show that p73 regulates endothelial junction morphology and stability during sprouting angiogenesis, being essential for the endothelial barrier maintenance. p73 deficiency, as well as TAp73-specific knockout (KO), results in hemorrhages and vascular hyperpermeability. Mechanistically, we propose that TAp73 modulates transcriptional programs involved in the regulation of cellular adhesion and blood vessel morphogenesis. We identified AMOT as a direct transcriptional target of TAp73 and one of p73 downstream mediators in the regulation of EC junction dynamics.

Results

p73 regulates endothelial junction morphology and stability during sprouting angiogenesis and TAp73 loss leads to hemorrhages and hyperpermeability

We sought to investigate whether p73 maintains the vascular structure through the regulation of EC junctions using mouse retinas to model physiological angiogenesis *in vivo* (Uemura *et al*., 2006). Adherens junction (AJ) morphology was analyzed in whole-mount retinas from wild type (WT) and *Trp73*$^{-/-}$ mice (p73KO) at post-natal day 7 (P7), when secondary sprouting will lead to the vascularization of deeper layers of the retina (Roca and Adams, 2007). The analysis of Vascular Endothelial Cadherin (VE-Cadherin) staining revealed profound differences in the arrangement of EC within p73-deficient vessels. In WT-retinas, VE-Cadherin delineates junctions that were thin, and mostly linear and continuous in all isolectin B4 positive (IB4+) vessels (Figure 1A, white arrows). On the contrary, in p73KO-retinas the EC junctions were tortuous with interrupted VE-Cadherin staining (yellow arrows). In few WT-vessels with decreased caliber we detected unicellular segments lacking VE-Cadherin (Figure 1A, white arrowhead) that probably reflect regressed vessels (Franco *et al*., 2015). However, in p73KO-retinas we observed many IB4-segments lacking VE-Cadherin staining (yellow arrows), even in multicellular vessels of normal caliber (blue arrowheads), which was indicative of increased vessel regression and defects in the establishment of multicellular tubes (Sauteur *et al*., 2014). On the leading front of the retinas, the defective p73KO

sprout morphology frequently correlated with aggregations of IB4-EC close to sprouts with very little VE-Cadherin (Figure 1A, blue arrows), arguing that the migration and/or the rearrangement of EC are perturbed in p73-defective vessels, and suggesting that vessels may have failed to anastomose or stabilize connections following sprouting, in line with previous reports (Fernandez-Alonso *et al*., 2015). This defects in vessel morphology were coupled to defects in function, since p73KO and TAp73KO retinas, but not DNp73KO, exhibited large hemorrhages at the angiogenic front and at the vascular network in the remodeling retina plexus (Figure 1B). Altogether, these data indicate that p73, TAp73 in particular, is necessary for the establishment of endothelial intercellular junctions and for junctional integrity *in vivo* regulating the rearrangements of EC whilst preventing bleeding in developing vessels, while DNp73 is dispensable for this function.

To further investigate this process, we analyzed endothelial sprouting using a 3D-differentiation model from pluripotent stem cells. WT- and p73KO-induced pluripotent stem cells (iPSCs) were differentiated via embryoid body (EBs) formation and IB4-positive vascular sprouts were examined (Figure 2A). WT-sprouts established a front-rear polarity at the leading edge (Lizama and Zovein, 2013), where tip cells adopted a finger-like shape with slightly low levels of VE-Cadherin that appears mainly cytoplasmic (Figure 2A, white arrow). The polarized rear-end of this cell was associated to a stalk cell via AJs, where VE-Cadherin tightly localized with β-catenin (Figure 2A, yellow arrow). In the p73KO-EBs, the few IB4-sprouts that could be noticed had completely altered junctional morphologies, with VE-Cadherin and β-catenin localizing scattered through the cytoplasm of the EC, independently of the cell position, and lacking front-rear polarity (Figure 2A, red arrows).

Tip cells in WT-sprouts (Figure 2B, white dashed arrow and yellow dashed box magnification) directed cell migration at the leading cell pole through the formation of thin filopodia (yellow arrows) and stress fiber formation (yellow arrowheads). In the center of the sprout (blue dashed box magnification), stalk cells established AJs with a linear VE-Cadherin pattern that strongly interacted with F-actin (white arrows) and displayed junction-associated branched actin filaments (white arrowheads). On the contrary, p73KO cells showed no polarization, with an increase in actin bundles forming stress fibers (Figure 2B, red arrows) and a little or no branched actin at cell junctions (red arrowheads), in comparison with control cells.

To gain insight into TAp73 as the isoform involved in the regulation of endothelial sprout formation and intercellular junctional dynamics, we used mouse embryonic stem cells

(mESC) with specific inactivation of the TAp73 (E14-TAp73KO, (López-Ferreras et al., 2021). Lack of TAp73 under 3D-differentiation conditions, strongly impaired the formation of new sprouts when compared to WT (Figure 2C, red and white dashed arrows, respectively). Nevertheless, the effect is less dramatic than in the total p73KO-EBs, since some ERG-positive sprouts were observed in TAp73KO-EBs (Figure 2C, right panels). WT-EC established sharp AJs with linear VE-cadherin/β-catenin colocalized staining (Figure 2C, white arrows). However, in TAp73KO sprouts VE-Cadherin staining was attenuated and appeared as dots scattered through the cytoplasm (blue dashed box magnification) and no proper AJs were observed. Few EC, mostly located at the base of the sprout, displayed intercellular β-catenin staining (red arrows), but the majority displayed thick intercellular accumulation of β-catenin (red arrowhead). Altogether, the *in vitro* results support our *in vivo* data indicating that TAp73 isoform is required for the establishment of endothelial intercellular junctions and proper vascular morphogenesis.

Subsequently, we sought to address the effect of p73 knockdown (p73KD) in the establishment of intercellular junctions in Human Umbilical Vein Endothelial Cells (HUVEC). Even though TAp73 levels in HUVEC are low, it should be noted that *TP73* gene silencing (+shp73) was robust (Figure 3A, right panel), either with respect to non-infected control cells (CTR) and to cells transduced with an empty vector (VECTOR). As shown in Figure 3A (left panel), VE-Cadherin staining revealed strong alteration of AJ´s morphology after p73KD. To accurately describe these differences, we took advantage of previous studies that had correlated AJ's morphology with cellular activities (Cao *et al*., 2017). In that work, straight or thick linear junctions were associated with stalk cell behavior, serrated junctions (VE-Cadherin fingers herein) correlated with actively rearranging cells, and reticular and thick/reticular corresponded to junction associated intermediate lamellipodia (JAILs) critical for cell migration and monolayer integrity (Neto *et al*., 2018). We analyzed the distribution of junctional categories after p73KD and observed that CTR and VECTOR cells frequently showed VE-Cadherin and actin plaque-like structures, JAILs, at the cell junctions (Figure 3B, green and pink arrows and bars). They also establish straight and thick junctions (purple and orange arrows) which maintain junction-associated actin filaments (JAAFs) and are associated to stalk cell behavior. VE-Cadherin fingers, which are associated with increased permeability in cell monolayers (Hayer *et al*., 2016), were present in lesser proportion in control monolayers (yellow bars). Strikingly, p73KD (+shp73) resulted in a sharp increase of fingers (yellow arrows and bars), suggesting possible defects in paracellular permeability. Furthermore,

p73 silencing resulted in a highly significant decrease in linear junctions and JAILs (green and pink bars), the latter required to maintain junction integrity even under sub-confluent conditions (Abu Taha and Schnittler, 2014). In line with this, p73KD led to junctional breaks in the monolayer (Figure 3B, white arrows). Immunostaining for F-actin in p73KD cells confirmed the increase in actin bundles appearing as stress fibers, and a decrease in branched actin networks, compared to control cells (Figure 3C). Our observations demonstrate that p73 is involved in the remodeling of endothelial junctions and is required for the formation of JAIL and the repression of VE-Cadherin fingers formation.

We hypothesized that the endothelial junctional alterations observed upon p73KD would translate into functional defects. In accordance with this, we measured a significant increase in transendothelial permeability to dextran molecules in p73KD cells compared to the control (Figure 3D). To further confirm p73KD effect on endothelial barrier function, HUVEC monolayer barrier integrity was monitored in real-time by transendothelial electrical resistance (TEER) measurements (Figure 3E). We observed significantly decreased TEER in p73KD, compared to CTR and VECTOR cells. TEER results obtained with ECIS can be mathematically modeled and separated into specific values, which reflect the contribution of various physiological parameters to changes in barrier function (Colás-Algora *et al*., 2020). p73KD significantly reduced Rb values, which measure paracellular permeability, but have no effect on alpha values, which reflect cell–matrix interactions, or in cell membrane capacitance, suggesting that the main effect of p73 downregulation, under the tested cell culture conditions, is the disruption of cell–cell junctions that control paracellular permeability. Altogether, our data strongly demonstrate that p73 plays a predominant role in maintaining the integrity of the endothelial barrier in the absence of any stimuli.

TAp73 orchestrates transcriptional programs involved in the regulation of cell-cell adhesion during blood vessel morphogenesis

To elucidate the underlying mechanism of p73 regulation of intercellular junctions, we made use of RNA-seq analysis in the p73KO-iPSCs. These cells exhibit defective intercellular junctions (Martin-Lopez *et al*., 2017) that can be restored by TAp73 expression (Supplementary Figure 1A and B and (Martin-Lopez *et al*., 2017)), making them a valuable model to compare the transcriptome of p73KO-iPSCs transfected with an empty vector (*Trp73-/-* cells) with those after TAp73 re-expression (+TAp73). The DESeq2 analysis identified 301 differentially expressed genes (DEGs) with a p-adj<0.05 (Supplementary Table 1); among these, we focused our attention on the 235 up-regulated

genes. Gene Ontology (GO) analysis and functional annotation clustering using DAVID Bioinformatics Resources 6.8 revealed the involvement of DEGs in biological processes (BPs) such as development, cell motility, blood vessel morphogenesis, cell-cell adhesion and actin filament organization, among others (Figure 4A-left graph and Supplementary Table 2). Indeed, some of the GO terms with the higher fold enrichment (FE) related to cell junction organization (GO:0034330, FE= 5.97, FDR 1×10^{-3}), while the key terms based on high significance corresponded to tissue development (GO:0009888, FE=3.28, FDR 1.77×10^{-17}) (Supplementary Table 2). These findings emphasize the important role of p73 during development (Maeso-Alonso *et al*., 2021, Nemajerova and Moll, 2019) and are consistent with previous reports of p73-mediated regulation of cell migration (Fernandez-Alonso *et al*., 2015, Landré *et al*., 2016), actin cytoskeleton dynamics (Fuertes-Alvarez *et al*., 2018), cell adhesion gene networks in murine granulosa cells (Santos Guasch *et al*., 2018) or VEGF (vascular endothelial growth factor) and TFG-β (transforming growth factor-β) signaling (Fernandez-Alonso *et al*., 2015, Stantic *et al*., 2015).

To reinforce our hypothesis that p73 exerts a role on sprouting angiogenesis through the regulation of cell junctions, we analyzed DEGs from the clusters "cell-cell adhesion" and "blood vessel morphogenesis" and generated an enrichment map to provide a more meaningful view (Figure 4A, right graph). The "cell-cell adhesion" cluster contained 44 DEGs and approximately half of them (47%) were common to the four GO terms strongly associated to this cluster (FDR ranging from 1.65×10^{-12} to 3.09×10^{-7}). Similarly, the "blood vessel morphogenesis" cluster comprised 53 DEGs, with one third of them shared by all the BPs included in the cluster (FDR ranging from 5.23×10^{-9} to 8.08×10^{-3}), altogether suggesting that there is a preserved gene set which is central to the establishment of cell-junctions and the formation of blood vessels and that is regulated by p73.

To further support these data, we revisited a published RNA-seq study in mESCs, comparing parental E14TG2α cells to E14-TAp73KO, either under proliferation conditions (Day 0, D0) or after three days of EB-induced differentiation (D3), when TAp73 is known to be upregulated (López-Ferreras *et al*., 2021). To narrow down the list of significant GO terms at D3 and reduce functional redundancies, we performed a clustering analysis (Figure 4B, left graph) which again disclosed BPs significantly (FDR<0.05) associated with development, cell communication, cell-cell adhesion and blood vessels morphogenesis. Not surprisingly, other highly significantly enriched BPs

were those related to the regulation of "cell death", which is intertwined with the canonical functions of this gene family (Pietsch *et al*., 2008); furthermore, p53 and p73 have been reported as major players for differentiation-induced apoptosis in mouse ESCs (He *et al*., 2016). The involvement of DEGs in "metabolic processes" was also underlined in the GO analysis. This previously characterized p73 function (Agostini *et al*., 2016, He *et al*., 2015) has been primarily linked to the tumour suppressive role of p53 family members (Napoli and Flores, 2017); however, in embryonic stem cells, where metabolic plasticity is considered critical for stem cell function and fate (Tsogtbaatar *et al*., 2020), p73 role remains to be addressed.

Interestingly, concomitantly with the reported TAp73 upregulation from D0 to D3 (López-Ferreras *et al*., 2021), the enrichment score (ES) of the BP-clusters in mESCs increased (Figure 4B, right graph). In the case of "blood vessels morphogenesis", the ES at D3 almost tripled the value at D0, highlighting the relevance of p73 in the regulation of this process. The molecular interaction networks (Figure 4C) reaffirmed the higher fold enrichment at D3 with regard to D0, together with an increase in both the statistical significance of the BP associations and in the number of shared genes within the GO terms of the clusters. Thus, altogether, these data strengthen the idea of p73 as a regulator of the vascular architecture through the control of transcriptional programs involved in cell junction establishment.

To identify possible p73-effector targets involved in this regulation, we performed a comparative analysis using: i) the DEGs from the above-mentioned experiments; ii) published transcriptomic data of upregulated DEGs after TAp73 expression in p73KO mouse epithelial granulosa cells-MGCs (Santos Guasch *et al*., 2018); and iii) a list of p73 putative targets identified by Chromatin immunoprecipitation sequencing (ChIP-seq). To obtain the latter list, GSE15780 data set from a TAp73 inducible cell line (Koeppel *et al*., 2011) was retrieved from ReMap (Chèneby *et al*., 2020), and peak annotation analysis was performed including transcription start sites (TSS) and enhancers. Venn diagrams showed 74 genes that overlapped between these data sets for the iPSC model and 184 genes in the case of E14-TAp73KO model (Figure 4D). Among these genes we found p73-transcriptional targets, like the E3 ubiquitin ligase *Mdm2* (Wang *et al*., 2001, Zeng *et al*., 1999), the regulator of cell cycle progression *Cdkn1a* (Zhu *et al*., 1998), the integrin *Itgb4* (Xie *et al*., 2018), the Jagged Canonical Notch ligand 1 *Jag1* (Fontemaggi *et al*., 2002), or the tripartite motif protein *Trim32* (Gonzalez-Cano *et al*., 2013). Finally, some of the overlapping genes have been predicted to contain p73 binding sites, such as, *Lima1*

(LIM Domain and Actin Binding 1) (Ohashi *et al*., 2017), *Pxn* (Paxilin), or the angiomotin family members *Amotl1* (Santos Guasch *et al*., 2018) and *Amot*. In particular, AMOT regulates endothelial cell-cell junction dynamics and integrates spatial cues from the extracellular matrix to establish functional vascular networks (Zhang *et al*., 2021) which makes it an interesting candidate as a p73-downstream effector in the maintenance of EC junctional integrity.

AMOT, a member of Angiomotin family, is a direct TAp73 transcriptional target

Expression analysis by qRT-PCR of WT-E14 mESCs during differentiation showed a strong upregulation of *Amot* expression and, to a much lesser extent, of *Amotl1* (Figure 5A), coinciding with an increase in TAp73 levels (Figure 5A' and Lopez-Ferreras *et al*., 2021). Enhancement of *Amot* expression was significantly hindered in the absence of TAp73 (Figure 5A, average 7.6-fold increase in WT vs. 2.7 in TAp73KO cells), suggesting that endogenous TAp73 might directly or indirectly regulate this gene. Supporting this idea, *Amot* expression was considerably lower in p73KO-iPSCs compared to controls, at RNA and protein levels (Figure 5B and C, respectively). It is noteworthy that AMOT isoforms, p130 and p80, increased with the culture confluency in WT-iPSCs but they were hardly detected in p73-deficient cells (Figure 5C). Moreover, ectopic expression of TAp73 induced AMOT p130 in p73KO-iPSCs (Figure 5D and E). TAp73-induction also correlated with *AMOT* up-regulation in another cell model (Figure 5F), the HA-TAp73β-TetOn inducible Saos-2 osteosarcoma cell line (Bálint *et al*., 2002), altogether backing up the idea that endogenous TAp73 regulates *AMOT*. Subsequently, we searched for p73 response elements (RE) within the *AMOT* proximal promoter and regulatory region using the JASPAR Core Vertebrata Database and identified a strong p73RE (score 13.3) located in intron 1 (Figure 5G). It is well documented that introns can contain enhancers, alternative transcription start sites, or transcription factor binding sites and, therefore, they have been shown to affect gene expression (Rose, 2019); indeed, a whole-genome map of p53 binding sites reported that almost a 10% of the RE in the p53 binding loci were located in introns (Wei *et al*., 2006). ChIP assays carried-out in HA-TAp73β-TetOn-Saos-2 cells confirmed a significant TAp73 interaction with the identified p73RE when HA-TAp73 was induced (Figure 5G, +DOXO), altogether demonstrating that *AMOT* is a direct TAp73 transcriptional target.

We next investigated whether p73 regulates *Amot* expression in IB4-positive EC generated from differentiated WT and p73KO-iPSCs (Figure 5H). Comparison of AMOT

p130 levels in non-endothelial iPSCs (EBs) and differentiated EC in the first passage (P1) revealed that AMOT p130 expression increased with differentiation in WT-EC (Pagliari *et al*., 2021, Zaltsman *et al*., 2019), but not in the absence of p73 (Figure 5I). A decrease in AMOT levels was observed in WT-EC with subsequent passages (P2 and P3), however, p73-deficiency always correlated with less AMOT. Moreover, in P7 mice retinal vessels, where *Amot* is ubiquitously expressed and is known to be essential for endothelial tip cell migration (Zhang *et al*., 2021), we detected very low levels of *Amot* in the absence of p73 (Figure 5J). Similarly, p73KD in HUVEC affected *AMOT* levels and localization (Figure 5K and L). AMOT was localized at the intercellular junctions in CTR and VECTOR EC (Figure 5L, white arrow), while in +shp73 cells it was scattered through the cytoplasm (dashed white arrow). Altogether, our data demonstrate that *Amot* is a TAp73 transcriptional target, and that p73 function is required to attain appropriate AMOT levels and localization in EC, suggesting that p73-deficiency might impinge upon AMOT function.

TAp73 regulates intercellular junctions through the regulation of AMOT levels

Even though, it is not yet clear how AMOT acts to promote angiogenesis *in vivo* (Zhang *et al*., 2021), one of its reported scaffolding functions is the sequestration of Yes-Associated Protein (YAP) to intercellular junctions (Zhao *et al*., 2011). YAP promotes both EC migration and barrier function maintenance (Neto *et al*., 2018) , and it relocates to the nucleus upon disruption of cell junctions or loss of VE-Cadherin (Choi *et al*., 2015). Thus, to address if p73 deficiency would impinge on AMOT downstream function, we analyzed YAP localization. Confocal microscopy analysis of HUVEC at the cell density conditions used for permeability assays (Figure 3D-E) showed a predominant cytoplasmic YAP staining in controls (Figure 6A, yellow arrows), with numerous cells exhibiting certain nuclear exclusion (white arrows). In p73-downregulated cells YAP distribution appears to be biased toward the nucleus (purple arrows) and cells had a significantly higher YAP nuclear/cytoplasmic ratio than controls. Similar results were obtained in the iPSC model where, as reported for mouse embryos and mESCs (Chung *et al*., 2016, Nishioka *et al*., 2009), the self-renewing cells at the center of WT colonies have YAP localized in the cytoplasm and in intercellular junctions (delineated by ZO-1), with 60% of their detected YAP outside the nucleus (Figure 6B, yellow arrows and graph), while YAP appeared nuclear in the polarized cells at the border of the colony (white arrows). Conversely, in p73KO cells, little YAP was localized at intercellular junctions,

and was mostly nuclear independently of the cell position (Figure 6B, blue arrows). This phenotype was rescued by transfection of knockout cells with a TAp73 expression vector, but not an empty vector, indicating that the defect on YAP cytoplasmic retention was due to TAp73-deficiency (Figure 6C, white arrowheads).

One of the proposed mechanisms to explain how cell-cell contact inhibition modulates localization of YAP/TAZ involves sequestration of YAP at junctional complexes by cell membrane proteins like AMOT (reviewed in (Cai *et al*., 2021). Thus, we sought to address if p73-downregulation, which results in decreased AMOT at intercellular junctions (Figure 5 L), would affect YAP cytoplasmic sequestration upon cell-cell contact. In sparse cultures, YAP protein was localized in nucleus and cytoplasm of controls as well as in +shp73 HUVEC (Figure 7A, yellow arrows). As expected, in confluent control cultures many cells displayed YAP nuclear exclusion (white arrows) and quantitative analysis showed a highly significant decrease of the YAP nuclear/cytoplasmic ratio when comparing low density conditions (1.6 ratio in VECTOR cells) to high density monolayers (1.1 ratio). Conversely, in in +shp73 EC we detected little nuclear exclusion (yellow arrows) upon confluency, and the nuclear/cytoplasmic ratio barely changed between low- (1.6 ratio) and high-density conditions (1.5 ratio), demonstrating that p73 function is part of the cellular mechanism mediating YAP sequestration upon cell-cell contact. Next, we ask whether p73-downregulation would impinge on YAP activity repression upon cell-contact inhibition. Unlike controls, in p73KD cells there was no significant change in the expression levels of canonical YAP/TAZ targets genes, like *CTGF, ANKRD1* or *CYR61,* between high- and low-density conditions (Figure 7B).

To clearly evidence that TAp73 regulates intercellular junctions, at least in part, through the regulation of AMOT levels, we attempted to rescue the endothelial junctional defects induced by the p73KD by stabilizing endogenous AMOT protein levels using a Tankyrase inhibitor (XAV939) (Wang *et al*., 2015). XAV939 treatment of p73KD cells resulted in an increase in AMOT levels and restored its intercellular junction localization (Figures 8A, white arrows). This correlated with a change in YAP localization, increasing YAP nuclear exclusion (dashed yellow arrows) and lowering the nuclear/cytoplasmic ratio, now like controls (Figure 8A). VE-Cadherin staining demonstrated that in treated p73KD cultures AMOT colocalized with VE-Cadherin, restoring the morphology of AJs (Figures 8B yellow arrows). Furthermore, AMOT stabilization significantly recuperated the formation of reticular junctions (JAILS) and reduced the formation of fingers in the

treated p73KD HUVEC monolayers (Figure 8B, lower panel), suggesting that the endothelial junctional dynamics and integrity were restored. Altogether these data unequivocally demonstrate that p73 regulates intercellular junction dynamics, at least in part, through the regulation of AMOT levels.

Discussion

The present study aimed to provide a deeper understanding of the mechanisms by which p73 regulates sprouting angiogenesis and demonstrates that p73, and TAp73 in particular, regulates endothelial junctional dynamics being essential for the maintenance of the endothelial barrier.

Endothelial junction integrity is regulated by proteins that form adherens and tight junctions (Claesson-Welsh *et al*., 2021). In particular, the intracellular complex of VE-Cadherin and catenins (which bridge cadherin to the actin cytoskeleton) are essential for junctional integrity (Claesson-Welsh *et al*., 2021). The idea of an interactive regulation between VE-Cadherin-mediated cell adhesion and actin dynamics in the control of barrier function has been previously introduced (Abu Taha and Schnittler, 2014). Thus, reduction of JAILs affects VE-Cadherin remodeling (Cao and Schnittler, 2019) and has been linked to decreased permeability in cultured EC (Breslin *et al*., 2015). Accordingly, p73 requirement for JAIL formation would intertwine with TAp73 modulation of transcriptional programs regulating actin cytoskeleton dynamics (Fuertes-Alvarez *et al*., 2018). Our observations not only reveal that p73 function is required for the formation of JAIL, but also to regulate the formation of fingers, linking p73 function to the maintenance of the vascular barrier. In this regard, we demonstrate that p73 plays a predominant role in maintaining the integrity of the endothelial barrier in the absence of any stimuli.

Endothelial barrier integrity is fundamental to ensure vascular and tissue homeostasis; consequently, in many diseases, the vascular barrier disintegrates, and leakage may become chronic. In cancer, blood vessels undergo changes fostered by the abnormal tumor microenvironment, including defective endothelial junctions that leads to increased permeability and leakage (Claesson-Welsh, 2015). Based in our data it is feasible to speculate that p73 deregulation might play a role in the chronic vascular hyperpermeability associated with pathological tumor angiogenesis (Nagy *et al*., 2012). However, future experiments will be required to address this point.

There is increasing evidence that endothelial junctions may play a coordinating role in angiogenic sprout formation, by polarizing the activity of the migration machinery and maintaining sprout cohesion (Szymborska and Gerhardt, 2018). p73 requirement for the establishment of endothelial junction morphology and stability during sprouting angiogenesis is supported by the data obtained in the 3D-endothelial differentiation models which have been shown to recapitulate the physiological steps of developmental vasculogenesis and sprouting angiogenesis (Jakobsson *et al*., 2007). Lack of p73, and TAp73 in particular, strongly impaired the formation of endothelial sprouts and the establishment of AJs, supporting TAp73 leading role for the establishment of intercellular junction in endothelial cells. Nevertheless, the observed effect is less dramatic than the one obtained after the total elimination of *TP73*, confirming the requirement of DNp73 pro-angiogenic function for a complete vascular morphogenesis process, in agreement with previous work that identified DNp73 as the isoform that governs EC migration and assembly of 2D tubular structures in HUVEC (Fernandez-Alonso *et al*., 2015). Even though TAp73 and DNp73 could have proangiogenic functions, it has been proposed that there may be differences in the mechanism by which they exert their activation and promotion of angiogenesis (Sabapathy, 2015). Our data *in vivo* also support this scenario, since DNp73 was dispensable for the integrity of endothelial junctions in mice retinal vasculature, while lack of TAp73 lead to functional defects.

To unravel the underlying mechanism of p73 regulation of intercellular junctions, we made use of transcriptome analysis in p73KO-iPSCs. Lack of p73 in this cellular model results in defective intercellular junctions that can be restored by TAp73 re-expression. In agreement with the proposed function of p73 as a tissular architect (Maeso-Alonso *et al*., 2021) and supporting that p73 exerts a role on sprouting angiogenesis through the regulation of cell junctions, GO analysis revealed that TAp73 modulates transcriptional programs involved in the regulation of cellular adhesion, developmental morphogenesis, and blood vessel morphogenesis. Similar results were obtained from a published RNA-seq study in mESCs, comparing parental E14TG2α cells to E14-TAp73KO cells (López-Ferreras *et al*., 2021). After performing a comparative analysis using several published transcriptomic data and a list of p73 putative targets identified by ChIP-seq, we focus our interest on AMOT, a member of the angiomotin family which is required for proper TJ and AJs activity (Bratt *et al*., 2005). Junction-associated proteins like AMOT, which localizes at the leading edge of migrating cells as well as at cell contacts, are involved in the regulation and coordination of front–rear polarity and collective migration and in

preserving the sprout cohesion (Aase *et al*., 2007, Ernkvist *et al*., 2009, Zheng *et al*., 2009). AMOT is also involved in the control of the vascular permeability (Bratt *et al*., 2005). Interestingly, *Amot*-deficient stem cells do not form sprouts in 3D endothelial differentiation assay (Aase *et al*., 2007), which phenocopies p73KO-iPSC (Fernandez-Alonso *et al*., 2015). We identified *AMOT* as a direct TAp73 transcriptional target and showed that its expression correlated with TAp73 levels not merely in endothelial cells *in vitro*, but also in the retina model *in vivo.* According to these results, downregulation of p73 expression results in lower levels of AMOT that appear scattered through the cytoplasm, rather than localized at intercellular junctions. Finally, the stabilization of endogenous of AMOT levels in p73KD EC by the tankyrase inhibitor treatment (Wang *et al*., 2015) restored the junctional defects caused by p73-inactivation, altogether conclusively demonstrating that p73 regulates intercellular junction dynamics, at least in part, through the regulation of AMOT.

In HUVEC, impairment of p73 function not only impinged in *Amot* expression, but also hindered AMOT downstream functions, like YAP cytoplasmic sequestration. However, it is important to keep in mind that YAP and p73 functional interaction is complex. YAP interacts with p73 and acts as its coactivator in pro-apoptotic genes; in turn, p73 expression is essential for the recruitment of YAP to PML-nuclear bodies following DNA damage (Conforti *et al*., 2012, Strano *et al*., 2005). Downregulation of p73 in HUVEC cultured at low density, when the Hippo signaling is turned “off”, resulted in lower expression levels of canonical YAP/TAZ targets than in controls cells cultured under the same conditions, suggesting that impaired p73 function could affect YAP activity at several levels. In the same line, members of the Transcriptional Enhancer Factor Domain (TEAD), considered as the primary axis through which YAP/TAZ regulate transcription (Hooglugt *et al*., 2021), are downregulated DEGs in TAp73KO-E14 mESCs (e.g. *Tead3*, p-adj = 7.07×10^{-5}; log2FC = -1.17; data analysis from Lopez-Ferreras *et al*., 2021). Thus, it is fairly possible that lack of p73 could affect YAP activity at many levels, independently of AMOT and a deeper analysis, which lays out of the scope of this study, would be required to untangle YAP/p73 functional interaction.

The present work contributes to the landscape of p73 function in angiogenesis by presenting a comprehensive study in healthy endothelial cells which express physiological *TP73* levels, providing an understanding of the mechanism by which p73 regulates intercellular junction dynamics in ECs. We propose that TAp73 is essential for the establishment and maintenance of EC junctions and that it carries out this function

through the regulation of transcriptional programs involved in cellular adhesion and blood vessel morphogenesis. Among the effectors of p73 regulation of endothelial junction dynamics, we identified *AMOT* as a direct p73 transcriptional target. These data allow us to upgrade and uncouple p73 function in angiogenesis and vascular morphogenesis in two axes. On one hand, the regulation of proangiogenic transcriptional programs in which DNp73 acts as a positive regulator in endothelial and tumor cells through the regulation on VEGF-A/Angiogenic genes as well as TGFβ1-signalling, while TAp73 has a cellular-context dependent bimodal function regulating these pathways. On the other hand, TAp73 works as a positive regulator of vascular architecture transcriptional programs, like cell-cell adhesion and actin dynamics, including *Amot* regulation.

Together, our results redefine the role for TAp73 in promoting EC rearrangements during sprouting angiogenesis through the regulation of junctional dynamics. Conceptually, the linking of p73 role in angiogenesis with its modulation of actin and junctional dynamics seems well suited to achieve vascular homeostasis and endothelial barrier functional integrity as part of p73 function as a tissular architect.

Material and methods

Mice husbandry, animal breeding and genotyping

Trp73$^{-/-}$ mice (p73KO) were obtained by crossing heterozygous mice for *Trp73* on a mixed C57BL/6 background (Yang *et al*., 2000). DNp73 mutant mice (DNp73KO) and TAp73 mutant mice (TAp73KO) have been described before (Tissir *et al*., 2009, Tomasini *et al*., 2008). Male and female mice, obtained from several litters, were used for the experiments. Genotyping of animals was performed by PCR analysis according to (Tissir *et al*., 2009, Yang *et al*., 2000, Tomasini *et al*., 2008). All animal experiments were carried out in agreement with European and Spanish regulations on the protection of animals used for scientific purposes (Council Directive 2010/63/UE and RD 53/2013, respectively) with the appropriate institutional committee approval.

Retina dissection and flat-mount preparation

Postnatal mice on day 7 (P7) were either decapitated or fully anesthetized and euthanized by trans cardiac perfusion. Animals were perfused with 1X PBS until the draining blood became clear, followed by fresh fixative perfusion (1% paraformaldehyde -PFA-, 0.1% triethanolamine, 0.1% Triton X-100 and 0.1% Nonidet^{TM} P-40 in 1X PBS at pH 7.4).

After that, eyes were enucleated and post-fixed for 2h at room temperature (RT). Retinas from non-perfused mice were dissected, fixed with 4% PFA during 40 min and stained immediately.

For wholemount staining, retinas were blocked for 2 h at RT with Buffer B (0.5% Triton X-100, 0.05% Na-Deoxycholate, 1% bovine serum albumin -BSA-, 2% fetal bovine serum -FBS- and 0.02% Sodium Azide in 1X PBS at pH 7.4). Afterwards, primary antibodies were added: VE-cadherin (BD #555298, Clone 11D4.1, 1:100 dilution, retinas from perfused mice) or TER119 R&Dsystems (#MAB1125-SP, 1:100 dilution, retinas from non-perfused mice). Samples were incubated at 4 ºC overnight (o/n). The following day, retinas were washed with 0.2% Triton X-100 and incubated with the secondary antibody (Donkey anti-Rat Alexa Fluor 488, Invitrogen, # A21208). All antibodies were diluted in Buffer B/1X PBS solution (1:1). Then, retinas were washed twice in PBLEC buffer (0.1 mM CaCl2, 0.1 mM MnCl2, 0.1 mM MgCl2, 1% TX-100 in PBS, pH 6.8) followed by incubation with 2 µg/ml biotin-conjugated isolectin B4 (IB4, Sigma-Aldrich, #L2140) in PBLEC, at 4 ºC o/n. Retinas were washed with 1X PBS and subsequently incubated with 4 µg/ml Streptavidin-Alexa555 (Invitrogen, #S32355). Finally, the retinas were mounted with Fluoromount-G™ (Electron Microscopy Sciences, # 17984-25).

iPSCs and mESCs culture and iPSCs transfection

Mouse wild type (WT) and p73KO-induced pluripotent stem cells (iPSCs) were previously generated from early passage murine embryonic fibroblasts (MEFs) from various WT or p73KO embryo littermates (E13.5 embryos, C57BL/6 background) (Martin-Lopez *et al*., 2017). iPSCs were cultured on MEFs feeder cells (5×10^4 cells/cm^2) in Dulbecco´s Modified Eagle Medium (DMEM, Sigma-Aldrich, #D5671) supplemented with 15% FBS, 2 mM L-glutamine, 1 mM sodium pyruvate, 1 mM nonessential amino acids, 0.1 mM β-mercaptoethanol and 1000 U/ml Leukemia Inhibitory Factor (LIF, Millipore, #ESG1107).

E14TG2α mouse embryonic stem cells (mESCs, E14-WT) were kindly provided by Dr. Jim McWhir (former researcher at Roslin Institute, Edinburgh, Scotland, UK) and E14-TAp73KO were generated by gene editing (López-Ferreras *et al*., 2021). Both cell lines were cultured on 0.1% gelatine-coated plates (10^5 cells/cm^2) in Glasgow Minimum Essential Medium (GMEM, Sigma-Aldrich, # G5154) supplemented with 10% FBS, 2 mM L-glutamine, 1 mM sodium pyruvate, 1 mM nonessential amino acids, 0.1 mM β-

mercaptoethanol and 500 U/ml LIF (Millipore, #ESG1107). All cell lines were cultured at 37°C in a humid atmosphere of 5% CO_2.

For transfection experiments, iPSCs were seeded (3.7×10^4 cells/cm^2) on Matrigel™ (Corning, #356231) coated plates or on coverslips (Sarstedt, #831840002). Cells were transfected with pcDNA-CMV-HA-TAp73 or empty vector using Lipofectamine™ 3000 Transfection Reagent (Invitrogen, # L300008). Transfection was performed following the manufacturer´s instructions as described in Fuertes-Alvarez *et al.*, 2018. Cells were analysed 24 h after transfection.

Endothelial differentiation and tube formation assays

Endothelial differentiation assays were carried out under two-dimensional (2D) or three-dimensional (3D) conditions. In the case of iPSCs, feeder cells were first removed. For that purpose, iPSCs colonies were disaggregated with Trypsin-EGTA and the obtained cell suspension was plated on 1% gelatine-coated dishes in EB medium (DMEM/GlutaMAX™-Gibco, #61965026, 25 mM HEPES, 1.2 mM sodium pyruvate, 19 mM monothioglycerol, 15% FBS), for 30 min at 37 °C, 5% CO_2. Non-attached cells were harvested and counted. Embryoid bodies (EBs) were then formed using the previously described hanging drop method (Li and Claesson-Welsh, 2009). A cell suspension of 6×10^4 cells/ml was prepared in EB medium and 20µl drops were placed onto a Petri dish lid and incubated for 4 days. Then, the EBs were flushed down from the lid with EB medium.

For 2D-differentiation, the EBs were disaggregated and plated (5×10^4 cells/cm^2) in EB medium supplemented with 50 ng/ml VEGF-A (Peprotech, #450-32), on 0.1% gelatine-coated plates (passage 0). Upon reaching 90% confluency (72-96h), cultures were trypsinised and re-plated on 0.1% gelatine-coated plates (Passage 1). This step was repeated twice (Passage 3).

For 3D-differentiation, EBs were embedded in a collagen I matrix composed of Ham's F12 medium (Sigma-Aldrich, #D8900), 6.26 mM NaOH, 12.5 mM HEPES, 0.073% NaHCO3, 1% GlutaMAX™ and 1.5 mg/ml collagen I (Advanced Biomatrix, #5005), supplemented with 100 ng/ml VEGF-A (Peprotech, #450-32).

To demonstrate the endothelial nature of the cells derived from 2D-differentiation experiments, the cells were stained with biotinylated IB4 (2 µg/ml, Sigma-Aldrich, #L-2140) as described below. 2D-Tube formation assays were also performed by seeding the obtained cultures in EB medium (12.5×10^4 cells/ml) over Matrigel™ (Corning,

#356231) coated plates. Images were acquired between 24-72 h with a phase contrast microscope (Leica, DMI 3000B) using 4x or 10x objectives (0.1 and 0.25 numerical aperture, respectively) and a digital camera (Leica, DFC 310FX).

Human Umbilical Vein Endothelial Cells (HUVEC)

HUVEC were isolated from the veins of umbilical cords kindly provided by Dr. Fernandez-Corona (Complejo Asistencial Universitario de León, CAULE) immediately after a scheduled birth, following an established protocol (Au - Davis *et al*., 2007). HUVEC were routinely maintained on 0.1% gelatine-coated flasks in endothelial basal medium, with full supplements (EBM Lonza, #CC3124), including bovine brain extract, hydrocortisone, human epidermal growth factor, ascorbic acid, FBS and gentamicin/amphotericin-B. Cells were used for experiments between passage 4 to 8.

HUVEC Knockdown studies

To knockdown p73 expression in HUVEC two different RNA interference approaches were conducted. When using synthetic small interfering RNA (siRNA), 5×10^5 cells per condition were centrifuged at 1,000 rpm for 10 min at RT and cell pellets were resuspended in a mixture containing 100 µl of Nucleofector® Solution (Amaxa® HUVEC Nucleofector® Kit, Lonza, #VAPB-1002) and 50 nM of the siRNA oligos, either Scrambled: 5´UAGCCACCACUGACGACCUdTdT3´, 5´dTdTAUCGGUGGUGACUGCUGGA3´, or sip73 (i4): 5´CCAUCCUGUACAACUUCAUGUG3´, 5´CAUGAAGUUGUACAGGAUGGUG3´) (Irwin *et al*., 2003). After nucleofection (Amaxa Nucleofector® Program A-034), cells were immediately seeded on 0.1% gelatine-coated 6-well plates and analysed after 48-96 h.

Lentiviral vector-based RNA interference was carried out with a combination of two lentiviral vectors encoding short hairpin RNA (shRNA) to enhance the silencing efficiency (LV pGIPZ shp73ex5, clone id V2LHS_69894 and LV pGIPZ shp73ex9, clone id V3LHA_330455). An empty pGIPZ vector (Dharmacon, # RHS4349) was used as control (VECTOR) (kindly provided by Dr. Benilde Jiménez Cuenca, Instituto de Investigaciones Biomédicas ‘Alberto Sols’, Madrid). Lentiviruses at a multiplicity of infection (MOI) of 20 (10 MOI of each plasmid in case of shp73) were added to the culture medium in the presence of 8 µg/ml polybrene for 8h, typically resulting in more than 95% transduced cells (EGFP-positive). After infection (72h), cells were seeded

either at 7,5 × 10^4 cells/cm^2 (high density) or 1 × 10^4 cells/cm^2 (low density conditions) on 0.1% gelatine-coated plates and were analysed 72-96 h after seeding. For tankyrase inhibition experiments, cells were treated 48-72h after seeding with 5µM XAV939 (Sigma-Aldrich, #CX3004) for 24 h.

HUVEC Endothelial barrier function assays

The *in vitro* vascular permeability assay (Millipore, # ECM644-24 wells) was performed following the manufacturer's instructions. Briefly, 2,5 × 10^5 cells were nucleofected and subsequently plated on the insert well (200µl). After 96 h, each insert was transferred to a fresh well plate and 150 µl of a 1:40 dilution of the provided FITC-Dextran was added. Then, 500 µl of media were added to each well of the Receiver Tray and incubated for 20 min at RT. The inserts were then removed and 100 µl of media from each well was transferred to a 96-black well plate for fluorescence detection (485 nm excitation/535 nm emission) in a plate reader (Biotek Synergy HT).

Trans-endothelial electric resistance (TEER) assays with an electric cell-substrate impedance sensing system (ECIS 1600R; Applied Biophysics) (Tiruppathi *et al*., 1992) were performed as described (Aranda *et al*., 2012, Fernández-Martín *et al*., 2012, Marcos-Ramiro *et al*., 2016). Briefly, 1,5 × 10^5 infected cells were plated onto 8W10E PET arrays (ibidi, #72001) and multifrequency measurement was carried out (ranges between 250 and 64000 Hz). ECIS software (Applied Biophysics) allowed mathematical modelling to separate TEER values into basolateral cell adhesion (alpha), which correlates with focal adhesion formation, cell membrane capacitance (Cm) and paracellular barrier resistance (Rb) (Giaever and Keese, 1991).

TAp73-inducible Saos-2 cell culture

The human cell line HA-TAp73β-Saos-2-Tet-On (Bálint *et al*., 2002), kindly provided by Dr. Karen Vousden (Cancer Research UK Beatson Institute, Glasgow), was cultured in DMEM supplemented with 10% FBS, 2 mM l-glutamine, and 100 U/mL penicillin–0.1 mg/mL streptomycin, at 37°C in a humid atmosphere of 5% CO_2. For TAp73 induction, 3 × 10^4 cells were seeded and 24h later, they were treated with 2.5 µg/ml of doxycycline (DOXO) for 36 h (Melino *et al*., 2004).

Immunofluorescence and confocal microscopy image acquisition

iPSCs and HUVEC were fixed with 3.7% PFA (or 3.7% PFA + 0.5% Tx-100 in the case of ZO-1 staining) during 15 min at RT. After a 1X PBS wash, PFA-fixed cells were incubated for 15 min in permeabilization buffer (0.5% Tx100 in 1X PBS). Cells were then blocked for 1 h using 10% normal goat serum in PBS and incubated with the corresponding primary antibodies at 4 ºC o/n (Table 1). The following day, cells were washed with 1X PBS and incubated for 45 min at RT with the secondary antibodies (Table 1). Nuclear counterstaining was performed with DAPI (1 µg/ml). Phalloidin-TRICT (Sigma Aldrich P1951; 1:100 dilution) and Phalloidin-488 (Thermo Fisher Scientific A12379, 1:100) were employed to label F-actin. Fluoromount-G™ (Electron Microscopy Sciences #17984-25) was used as mounting media.

For immunostaining of 3D-endothelial differentiated cells, fixation was carried out with 4% PFA for 30 min at RT, followed by blocking and permeabilization with 3% BSA, 0.2% Tx-100 in 1X PBS, for 1 hour at RT. Then, the general procedure described above was followed, except that incubation with secondary antibodies was performed at 4 ºC o/n. For IB4-labeling, cells were washed at RT in PBLEC buffer, followed by incubation with 2 µg/ml of biotin-conjugated IB4 (Sigma-Aldrich, #L-2140) in PBLEC, at 4 ºC o/n. Then, cells were extensively washed with 1X PBS at RT (5 x 30 min) and subsequently incubated with 4 µg/ml Streptavidin-Alexa555 (Invitrogen, #S32355).

Confocal microscopy images (8bits) were obtained in a Zeiss LSM800 Confocal Laser Scanning Microscope using 25x Plan-Apo/0.8 numerical aperture or 63x Plan-Apo/1.4 numerical aperture oil objectives at RT. In indicated cases, a 0.5 zoom was used. Confocal Z-stack images were acquired in all cases and stacks were z-projected to maximum intensity. Images were processed with the ZEN blue software.

Image analysis and quantification

For the quantification of *in vivo* permeability, a semi-automatic macro, designed with Image J/Fiji software, (Schindelin *et al*., 2012, Schneider *et al*., 2012) was applied to confocal z-stack pictures. Blood vessels were selected using the IB4-channel which was binarized with and automatic threshold. Blood vessel selection was overlapped with TER119 staining and “clear” or “clear out” options were used for outside or inside particle quantification, respectively. “Analyse particles” plug-in was used to count TER119-stained particles for each condition and particle percentage was calculated for each image.

At least three independent mice from each genotype were considered, and a minimum of four non-overlapping fields were quantified for each animal.

Cell junction morphology analysis was performed based on previous publications (Neto *et al*., 2018). Briefly, five morphological categories were defined: straight, thick, thick/reticular, reticular and finger-like. Each image was divided in 36 patches and one morphological category was manually assigned to each patch. Three independent transductions experiments were performed and ten pictures from each experiment were randomly selected and classified (n=30 pictures per condition).

For the quantification of YAP localization two different strategies, both based on Image J semi-automatic macros, were chosen. For HUVEC experiments, a Gaussian Blur filter ($\sigma = 2$) was applied to the DAPI channel and images were binarized using an automatic threshold. The "Analyse particles" plug-in was used to identify the number of cells in the image. Then, the cell region was drawn manually and selected. "XOR" option was used to subtract the nuclei selection from the cell region and obtain the cytoplasmic region. The mean intensity of YAP at nuclei and cytoplasmic region was measured. Three independent infections were performed and at least five pictures from each experiment (with a minimum number of 5 cells per picture) were randomly selected and quantified.

For iPSCs experiments, nuclei were selected using the DAPI channel which was binarized with an automatic threshold. Nuclei selection was overlapped with YAP staining and "clear" or "clear out" options were used for quantifying cytoplasmatic or nuclear mean fluorescence, respectively. For a more accurate calculation of the percentage of YAP fluorescence in each subcellular compartment, total YAP mean fluorescence was also determined. Three independent transfection experiments were performed using different clones per genotype. Eight pictures from each experiment were randomly selected and quantified ($n = 24$ pictures per condition).

RNA Sequencing (RNA-seq) and Transcriptome Data Analysis

Total RNA from p73KO-iPSCs (transfected with an empty VECTOR) and cells after TAp73 re-expression (p73KO-iPSCs+TAp73) was isolated using the RNeasy Mini Kit (Qiagen, #74106) following the manufacturer's instructions, and the quality was assessed using an Agilent 2100 Bioanalyzer (Agilent Technologies). Whole transcriptome sequencing from two biological replicates per condition was carried out at the Genomics and Proteomics Service of the National Centre for Oncological Research (CNIO, Madrid).

RNA-seq was conducted on the HiSeq Illumina and 20 million reads were generated for each library. Sequencing reads were aligned to the transcriptome with TopHat (v 2.1.1; http://ccb.jhu.edu/software/tophat/index.shtml) provided with known gene annotations and other transcript data (GTF file) taken from the Ensembl (release 84) gene set for the GRCm38/mm10 mouse genome assembly. Alignment data were quantitated with HTSeq (Anders *et al*., 2015). Differential gene expression analysis was subsequently performed with DESeq2 (Anders and Huber, 2010). Genes were assigned as differential expressed genes (DEGs) if they had an adjusted p-value < 0.05.

Gene ontology (GO) and Functional Annotation Clustering were performed using DAVID Bioinformatics Resources 6.834 (Huang *et al*., 2008, Huang *et al*., 2009), choosing level 3 of GO terms specificity. Clustering results were plotted using the ggplot2 library from R (3.5.1) Core Team (2014). Genes shared by the selected functional clusters were identified and the results were plotted with Cytoscape 3.7.2 (Shannon *et al*., 2003). Venn diagrams were created using BioVenn (http://www.biovenn.nl/) (Hulsen *et al*., 2008).

RNA isolation, reverse transcription, and quantitative real-time PCR (qRT-PCR)

Total RNA from dissected mice retinas or cultured cells was isolated using the RNeasy Mini Kit (Qiagen, #74106) and cDNA was synthesized using up to 1 µg of total RNA with the High-Capacity RNA-to-cDNA™ Kit (Applied Biosystems, #4387406). Gene expression levels were detected by qRT-PCR in a StepOnePlus™ Real-Time PCR System (Applied Biosystems) using FastStart Universal SYBR Green Master mix (Roche, #4913850001). All protocols were performed according to the manufacturer's instructions. Primers sequences are listed in Table 2. For gene expression analysis, relative expression values were calculated according to the $2^{-\Delta\Delta CT}$ Method (Livak and Schmittgen, 2001)

Chromatin immunoprecipitation assay (ChIP)

In silico prediction of the p73 responding element (RE) within the human *AMOT* gene was performed using the open access database for eukaryotic transcription factor binding profiles JASPAR (Mathelier *et al*., 2016). Matrix models MA0861.1 and MA0525.1 were applied, and a site with a score of 13.3 was selected for further in vitro analysis. Primers encompassing the p73RE in human AMOT gene were as follows: F →5'-TGTCCCCTTTTCTGCAGAGC -3´ and R→5'- GCTCCCCACTGACACGTTAA -3´.

ChIP analysis was carried out as previously described (Martin-Lopez *et al*., 2017) using HA-TAp73β-Saos-2-Tet-On cells. Samples were fixed with 1% formaldehyde for 10 min at RT. The reaction was stopped by addition of 125 mM glycine for 10 min at RT. Cells were washed with 1X PBS, collected with a rubber policeman and centrifuged at 1,500 rpm for 3 min at RT. The pellet was resuspended in 200 µl of lysis buffer (20 mM Tris HCl pH 8, 2 mM EDTA, 150 mM NaCl, 0.7% SDS) supplemented with a protease inhibitor cocktail (Calbiochem, #539131). The cell lysate was sonicated to an average size of 400 bp using a Bioruptor® Sonicator (Diagenode).

Chromatin was immunoprecipitated with the following antibodies: anti-HA (Y-11) (Santa Cruz Biotechnology, #sc805), anti-p73 (EP436Y) (Abcam, # ab40658) and anti-p53 (C-19) (Santa Cruz Biotechnology, #sc1311). Antibodies and cell lysates were incubated at 4 °C o/n prior to the addition of protein G-coupled magnetic beads (Dynabeads, Invitrogen, #10004D) for another 4 h at 4 °C. Negative controls were prepared by incubating parallel samples with non-immune rabbit IgG (Abcam, #ab171870).

Immuno-complexes bound to the beads were collected with the magnet DynaMag™ Magnetic particle concentrator (Dynalbiotech, #20.20) and were eluted from the magnetic beads with 200 µl of ChIP elution buffer (1% SDS; 50 mM Tris-HCl pH 7.5). The protein-DNA cross-links were reversed in elution buffer (1% SDS and 50 mM Tris-HCl), followed by RNAse treatment at 65°C o/n. The eluted material was incubated with proteinase K at 45°C for 3 h, and the DNA was purified using the QIAquick PCR Purification Kit (Qiagen, # 28704) and used for qPCR with FastStart Universal SYBR Green Master (Roche, #4913850001). The signals were normalized to the input (non-immune rabbit IgG immunoprecipitation).

Protein isolation and Western blot analysis

Cells were washed with cold 1X PBS and lysed at 4 °C for 30 min with EBC lysis buffer containing 50 mM Tris pH 8, 120 mM NaCl, 0.5% NP-40, and proteases inhibitors: 10 µg/ml aprotinin (Sigma-Aldrich, #A6279), 20 µg/ml leupeptin (Sigma-Aldrich, #L9783), 1 mM sodium orthovanadate (Sigma-Aldrich, #S6508) and 0.1 mg/ml sulfonylmethylphenyl fluoride (PMSF, Sigma-Aldrich, #P7626).

Protein samples (ranging between 20 and 100 µg) were subjected to SDS-PAGE and transferred to nitrocellulose membranes (Bio-Rad, #162-0115), using a Mini Trans-Blot ® Electrophoretic Transfer Cell (Bio-Rad) system. Membranes were incubated with rabbit anti- AMOT 1:600 (kindly provided by Dr. Lars Holmgren, Karolinska Institutet,

Stockholm, Sweden) or mouse anti-GADPH 1:1500 (Abcam, #ab8245), diluted in 2.5% non-fat dried milk/TBS-T (Tris Buffer Saline-0.05% Tween 20), at 4 ºC o/n with gentle agitation. After washing with TBS-T, membranes were incubated with 25 ng/ml horseradish peroxidase-coupled secondary antibody (Pierce, #31430 or #31460) in 2.5% non-fat dried milk/TBS-T for 1 hour at RT. HRP-conjugated proteins were visualized with Super Signal West-Pico Chemiluminescent Substrate (ThermoFisher Scientific, #34087), followed by membrane autoradiography.

Statistical analysis

Statistical analyses were performed using GraphPad Prism 9.3 software. Values were expressed as mean ± standard error of the mean (SEM). Differences were considered significant when $p < 0.05$ (*$p < 0.05$, **$p < 0.01$, ***$p < 0.001$). Data distribution was analysed in all cases, and non-parametric tests were applied when necessary. In the latter scenario, statistical differences were calculated according to Mann–Whitney tests or to Kruskal-Wallis test with Dunn's correction for multiple comparisons. For grouped data, a two-way analysis of variance (ANOVA) was carried out with Sidak´s or Tukey´s post hoc test to account for multiple comparisons. For the analyses of YAP localization after p73KD in HUVEC, the relative likelihood of sampling from a Gaussian versus a lognormal distribution was computed and log transformation was used to express the ratios between YAP fluorescence intensity in the nucleus versus cytoplasm. Thus,

Funding: This work was supported by Grants PID2019-105169RB-I00 (from Spanish Ministerio de Ciencia e Innovación cofinanced by FEDER funds) and LE022P20 (from Junta de Castilla y León) (to M.C.M.). L.M.-A. and J.V.-F. and are funded by Junta de Castilla y León. H.A.-O. and N.M.-G. are supported by a predoctoral scholarship from the Asociación Española contra el Cáncer (AECC).

Figure legends

Figure 1. TAp73 regulates endothelial cell junctions integrity during retinal sprouting *in vivo*. (A-B) Representative confocal microscopy images of vascular networks and leading edges from P7 WT, p73KO, TAp73KO **(B)** and DNp73KO **(B)** mice retinas labelled with IB4 (red), anti-VE-CADHERIN (green) **(A)** and anti-TER119 (green) **(B)**. **(A)** Images on the right correspond to a magnification of the indicated areas (dashed white square) that show linear intercellular junctions (white arrows) with unicellular segments lacking VE-CADH (white arrowhead) in WT vascular network's retinas, while lack of p73 in p73KO retinas results in vessels with interrupted staining (yellow arrows), including multicellular vessels (blue arrowheads), and aggregation of IB4-ECs (blue arrows). Retinas from at least three mice were analyzed in each experiment. Scale bar 20μm. **(B)** Vessel integrity was assessed by quantification of the percentage of TER119 positive cells localized inside or outside of IB4+ blood vessels (right panel). Bars represent mean percentage ± S.E (n>20 pictures from 3 separate mice per genotype). For each genotype, p value was calculated with respect to the value of WT littermates. ***p<0.001, ns: non-significant.

Figure 2. p73 is required for the establishment of endothelial cell-cell junctions during angiogenic sprouting *in vitro*. (A-C) Endothelial adherens junctions of IB4-positive (**A-B**) or ERG **(C)** vascular sprouts formed in WT and p73KO-iPSC **(A-B)** or E14-WT- and TAp73KO **(C)** EBs after 12 **(A-B)** and 21days **(C)** of 3D differentiation culture conditions were analyzed by VE-CADHERIN (blue) **(A-C)**, F-ACTIN (green) **(B)**, and β-CATENIN (green) **(A, C)** staining. Nuclei were counterstained with DAPI (yellow). Scale bar: 20 μm. The images below of each panel correspond to the magnifications of the areas marked with yellow or blue dashed squares. **(A)** Representative confocal images showed that WT tip cells (white arrow) have low cytoplasmic VE-CADH staining, while in stalk cells (yellow arrow) it is tightly co-localized with β-CATENIN forming AJ. p73-deficiency results in altered junctional morphology independently of the cell position (red arrows). **(B)** In WT sprouts tip cells (white dashed arrow) showed the formation of thin filopodia (yellow arrows) and stress fibers (yellow arrowheads) while in stalk cells AJs interact with F-ACTIN (white arrows) and displayed junction-associated branched actin filaments (white arrowheads). Lack of p73 leads to an increase in stress fibers (red arrows) and a decrease of branched actin (red arrowhead). **(C)** TAp73 is required for the establishment of appropriate AJs in ERG-positive sprouts compared to WT. Phase-contrast microscopy images of E14-WT and

TAp73KO after 21 days of in vitro 3D endothelial differentiation formed sprouts (white and red dashed arrows, respectively). Scale bar: 250μm. EGR-positive WT sprouts (right panel) establish sharp AJs (white arrows). In the absence of TAp73 only some EGR-positive cells at the base of sprout establish AJ (red arrows), but the rest have thick intercellular accumulation of β-CATENIN and no VE-CADH staining (red arrowhead). Images are representative of at least three independent experiments.

Figure 3. p73 regulates adherens junctions morphology and dynamics and monolayer permeability. (A-C) Representative confocal microscopy images of confluent HUVEC monolayers after either no infection control (CTR), infected with non-silencing empty vector (shRNA, VECTOR) or with shRNA targeting p73 (+shp73), and stained for VE-CADHERIN **(A** orange**; B, C** green) or F-ACTIN **(B, C,** red**)**. Nuclei were counterstained with DAPI (light blue) **(A, B)**. Scale bar: 20 μm. **(A)** VE-CADHERIN staining shows that p73-KD results in alteration of adherens junctional morphologies. TAp73 expression level was analyzed by qRT-PCR (n=3) after p73-KD (right graph). Bars represent mean ±S.E of 3 independent experiments. $^{**}p<0.01$, ns: no significant. **(B)** Morphological analysis of VE-CADHERIN labelled cell junctions in HUVECs after knocked down of p73. Representative patches (right panel) used for manual morphological classification of AJs in five categories: straight junctions (purple arrows), thick junctions (orange arrows), thick to reticular junctions (pink arrows), reticular junctions (green arrows) and fingers (yellow arrows). The images below correspond to the magnifications of the areas marked with white dashed squares. White arrows represent cellular gaps. Quantitative analysis of VE-CADHERIN cell junction morphology. Bars represent mean percentage ± S.E (n=30 pictures across three independent experiments). *p* values for each type of morphology were calculated between +shp73 and VECTOR values. There were no significant differences among the morphological types between CTR and VECTOR. $^{***}p<0.001$. **(C)** p73KD induces an increase in actin bundles (stress fibers), and a decrease in branched actin networks (F-ACTIN, red). Cell delimitation was determined by VE-CADHERIN (green) staining. **(D)** Permeability of p73KD HUVEC monolayers (i4) to 250 kDa fluorescent dextran molecules was significantly higher compared to no interfered (CTR) and scrambled control (SCR) (upper graph). TAp73 level expression was analyzed by qRT-PCR in each case (lower graph). Data are mean ±S.E of 3 independent experiments. $^{**}p<0.01$, ns: no significant. **(E)** ECIS analysis of the effect of p73KD (shp73) by TEER (Trans-endothelial electric resistance) measurement demonstrates that p73 is necessary for the integrity of intercellular junctions

that control paracellular permeability (n=3). ECIS mathematical modelling of the TEER analysis in yields three values: Rb values (left), Alpha values (center) and Cell membrane capacitance (right). Bars represent mean ± S.E of three independent experiments. ***p<0.001, ns: non-significant.

Figure 4. TAp73 is a central hub for the modulation of transcriptional programs involved in cellular junctions and blood vessel morphogenesis. Up-regulated DEGs (p-adj<0.05, log2FC>0) from iPSCs cells after TAp73 re-expression **(A,** left panel**)** and downregulated DEGs (p-adj<0.05, log2FC<0) from E14-TAp73KO cells under differentiation conditions at Day 3 **(B**, left panel**)** were analyzed with DAVID Bioinformatics Resources 6.8. Functional annotation clustering was performed, and the selected enriched clusters were represented. The number of terms that compose each cluster was indicated (f=number). (**B**, right panel) Enrichment Score (ES) Fold Increase between Day 0 and Day 3 for the selected clusters. **(A, C)** Network analysis of Cell-cell adhesion and Blood vessels morphogenesis clusters from iPSCs-RNA-seq **(A,** right panel**)** and E14-RNA-seq (**C**, Day 0 left panel, Day 3 right panel) were performed using Cytoscape 3.7.2. Nodes in the graph represent the categories/GO terms for each annotation cluster. The node color indicates the false discovery rate (FDR) for the association of the DEGs to each category, while the node size represents the Fold Enrichment of each term. The edges connect overlapping categories, and the edge thickness depicts the magnitude of the overlap as indicated in the figure legend. **(D)** Comparison of the upregulated DEGs from iPSCs-RNA-seq or the downregulated DEGs from E14-RNA-seq (Day 3) with previously published RNA-seq and ChIP-seq data from the indicated studies.

Figure 5. AMOT, a member of the Angiomotin family, is a TAp73 transcriptional target. *Amot* expression correlates with TAp73 levels in E14-WT and -TAp73KO after three days of differentiation conditions **(A, A'),** in WT and p73KO-iPSCs in basal conditions **(B, C)** and after ectopic expression of TAp73 both at RNA **(D)** and protein **(E)** levels, as well as after doxocyclin induction (+DOXO) in HA-TAp73β-Saos-2-Tet-On **(F)**. Values in A, A', B, C represent mean ± S.E of three independent experiments. * p<0.05, ** p<0.01, ***p<0.001, ns: no significant. **(G)** Schematic diagram of the human *AMOT* locus (ENSG00000126016). The direction of transcription is marked with a horizontal black arrow. Predicted p73 p73 response element (p73RE) matches to intronic sequence downstream exon 1, that contains the ATG sequence (green). Position of the p73RE is marked by an orange arrow (p73RE) and is identified with the number of base

pairs from TSS (Transcription Start Site) for the indicated transcript. Direct binding of TAp73 to this p73RE was analyzed by ChIP in HA-TAp73β-TetOn-Saos-2 before and after TAp73 induction by Doxycycline treatment (DOXO). ChIP was performed using isotypic-antibody (rabbit IgG) and anti-p53 as controls or anti-HA and anti-TAp73 specific antibodies. q-PCR using specific primers to amplify p73-RE of the human *AMOT* promoter were performed and the data were normalized to input chromatin samples of each case and to IgG values=1. **(H-L)** AMOT expression analysis in undifferentiated cells (EBs) and at various passages after endothelial differentiation (P1-P3). AMOT correlates with p73 status in IB4-positive endothelial cells derived from WT and p73KO-iPSC **(H-I)**, as well as in WT and p73KO mice retina **(J)** and in HUVEC cells after p73KD (+shp73) **(K-L)**. Bars represent mean values ± S.E. *$p<0.05$, ***$p<0.001$, ns: non-significant. **(H)** Representative phase-contrast and fluorescence microscopy images (staining with the endothelial marker IB4 after endothelial differentiation). Scale bar: 50 and 25 μm, respectively. Phase-contrast images of the tube formation assay on Matrigel. Scale bar: 25 μm. **(L)** p73KD decreases AMOT (green) levels and localization in HUVEC In CTR and VECTOR cells, AMOT is localized at the intercellular junctions (white arrows) while it is scattered through the cytoplasm in +shp73 cells (dashed white arrows). Nuclei were counterstained with DAPI (light blue). Scale bar 20 μm**.** Experiments were repeated three times per duplicate.

Figure 6. p73 regulates YAP localization at intercellular junctions. p73-deficiency results in altered YAP localization in HUVEC **(A)** and in iPSC **(B)** and ectopic expression of TAp73 can restore it **(B)**. **(A**) Representative confocal microscopy images of YAP (green) localization in HUVEC in either control (CTR) and VECTOR cells where YAP is predominantly cytoplasmic, and some cells exhibit nuclear exclusion (yellow and white arrows, respectively) or after p73KD (+shp73) where cells showed increased nuclear staining (purple arrows). F-ACTIN is visualized in orange and nuclei were counterstained with DAPI (pink). Scale bar: 20 μm. Quantification of YAP nuclei/cytoplasm ratio (right panel). The obtained data follow a logarithmic distribution, and each analyzed cell was represented as log10 (n>100 cells across three independent experiments). *p* value is indicated in the graph. **(B)** Representative confocal microscopy images of WT and p73KO-iPSC transfected with the indicated expression vectors. YAP (green) located in the intercellular junctions (yellow arrows) in self-renewing cells at the center of WT colonies and nuclear in cells at the border of the colony (white arrows) colocalizing with ZO-1 (red). p73-deficient cells displayed YAP at the nucleus (blue arrows) independently

of cell position. Ectopic expression of TAp73 restored YAP cytoplasmic retention and ZO-1 colocalization (white arrowheads). Transfected TAp73 (blue) was visualized using specific antibodies and nuclei were counterstained with DAPI (pink). **(B,** right panel**)** Quantification of the percentage of nuclear YAP localization in each condition. Bars represent mean percentage ± S.E (n>20 pictures across three independent experiments). ***p*<0.01, ****p*<0.001, ns: non- significant.

Figure 7. p73- deficiency impairs YAP cytoplasmic sequestration upon cell-cell contact in endothelial cells. (A) Analysis of YAP (red) localization in HUVEC at different density conditions (Low/High). Cell delimitation was discerned by β-CATENIN (green) staining. Nuclei were counterstained with DAPI (light blue). Scale bar: 20 µm. Under spars culture conditions (low density) YAP localized mainly at nucleus in all cells (yellow arrows). Upon contact inhibition (high density) many CTR and VECTOR cells displayed YAP nuclear exclusion (white arrows); however, p73KD cells (+shp73) showed little nuclear exclusion (yellow arrows) upon confluency. Quantification of YAP nuclei/cytoplasm ratio after p73 knockdown (+shp73) (right panel). The obtained data follow a logarithmic distribution, and each analyzed cell was represented as log10. (n>60 cells (Low-density) and n>100 (High-density) across three independent experiments). *p* value is indicated in the graph. **(B)** p73-downregulation impinge on the repression of YAP activity upon cell-contact inhibition. Expression levels of canonical YAP/TAZ targets genes: *CTGF, ANKRD1 and CYR61* were analyzed by qRT-PCR (n=3) after p73 knockdown (+shp73) in Low- and High-density conditions. qRT-PCR assays were repeated three times by duplicate across three independent experiments. Bars represent mean values ± S.E. * p <0.05, ** p < 0.01, *** p < 0.001, ns: non-significant.

Figure 8. AMOT is a TAp73 downstream effector during the regulation of endothelial cells junctions. (A-B) Stabilization of endogenous AMOT levels by XAV939 treatment restores the endothelial junctional defects induced by the p73KD. Representative confocal microscopy images of HUVEC after p73KD (+shp73) with and without XAV939 treatment (n=3). **(A)** XAV939 treatment restores AMOT (pink) levels and localization at intercellular junctions (white arrows) and correlated with a change in YAP (orange) localization in p73KD cells upon treatment, showed an increased YAP nuclear exclusion (solid and dashed yellow arrows, respectively). (**A**, low panel) Quantification of YAP nuclei/cytoplasm ratio after p73 knockdown and XAV939 treatment. The obtained data follow a logarithmic distribution, and each quantified cell was represented as log10. (n>100 across three independent experiments). *p* value is

indicated in the graph. **(B)** AMOT restoration (white arrows) also rescues the morphology of AJs as shown by VE-CADH (orange, yellow arrows) staining. **(B,** low panel**)** Quantitative analysis of VE-cadherin cell junction morphology in HUVEC after p73 knockdown and XAV939 treatment. Nuclei were counterstained with DAPI (blue). Scale bar: 20 µm. Bars represent mean ± S.E (n=30 pictures across three independent experiments). P values for each type of morphology were calculated between +shp73 and VECTOR values (***p<0.001) and between +shp73 cells with or without XAV939 treatment (###p<0.001). There were no significant differences among the morphological types between CTR and VECTOR.

Supplementary Figure 1 TAp73 overexpression can restore the adherens and tight junctions in p73KO-iPSCs. p73-deficiency results in an altered intercellular adhesions and ectopic expression of TAp73 restores them. **(A, B)** Representative confocal images of WT and p73KO-iPSC transfected with the indicated expression vectors. Adhesion proteins were visualized by staining with anti-β-CATENIN (**A**, red) and anti-ZO1 (**B**, red). Transfected TAp73 (**A**-green; **B**-blue) were visualized using specific antibodies. Scale bar: 10 µm.

Table 1. Primary and secondary antibodies used for immunofluorescence.

	Antibody	Host	Dilution	Manufacturer	Catalog Number
Primary	**E-cadherin (24E10)**	Rabbit	1/200	Cell Signalling	3195
	HA (F-7)	Mouse	1/200	Santa Cruz Biotechnology	sc-7392
	p73 (Ab-4)	Mouse	1/200	NeoMarkers	M-764-P
	VE-cadherin	Goat	1/100	R&D Systems	AF1002
	VE-cadherin (F8)	Mouse	1/500	Santa Cruz Biotechnology	sc9989
	YAP (63.7)	Mouse	1/100	Santa Cruz Biotechnology	101199
	ZO-1 (1A12)	Mouse	1/100	Thermo Fisher	339100
	β-Catenin (14)	Mouse	1/200	BD transduction lab.	61053
	Amot (D2O4H)	Rabbit	1/200	Cell Signalling	43130S
Secondary	**Alexa Fluor 488** anti Rabbit	Donkey	1/1000	Molecular Probes	A21206
	Alexa Fluor 488 anti Mouse	Goat	1/1000	Molecular Probes	A21131
	Alexa Fluor 546 anti Mouse	Donkey	1/1000	Molecular Probes	A10036
	Alexa Fluor IgG1 594 anti Mouse	Goat	1/1000	Molecular Probes	A21125
	Alexa Fluor 647 anti Mouse	Donkey	1/1000	Molecular Probes	A31571
	Alexa Fluor 647 anti Goat	Donkey	1/1000	Molecular Probes	A21447

Table 2: Primer sequences used for qRT-PCR.

Gene	Specie	Sequence	Reference
18S	Mouse	F 5′-AGTTCCAGCACATTTTGCGAG-3′	(Grespi and Melino, 2012)
		R 5′-TCATCCTCCGTGAGTTCTCCA-3′	
Amotl1	Mouse	F 5′-ATGTAGCCTCTGGAAGAGTGT-3′	Primer Bank Database ID: 26340072a1
		R 5′-TGAGTGAGGGTTTCCGTGGA-3′	
Amot	Mouse	F 5′-CCGCCAGAATACCCTTTCAAG-3′	Primer Bank Database ID: 23503333a1
		R 5′-CTCATCAGTTGCCCCTCTGT-3′	
TAp73	Mouse	F 5′-GCACCTACTTTGACCTCCCC-3′	(Tomasini *et al*., 2008)
		R 5′-GCACTGCTGAGCAAATTGAAC-3′	
18S	Human	F 5′-GGCGCCCCCTCGATGCTCTTA-3′	Primer Bank Database
		R 5′-GCTCGGGCCTGCTTTGAACAC-3′	
gaAMOT	Human	F 5′-ACCTCGTGAAGTCATCCTCCCA-3′	Primer Bank Database ID: 63252911c2
		R 5′-CCTCCGAATCTCGCCCTCTA-3′	
TAp73	Human	F 5´-GCACCTACTTCGACCTTCCC-3′	Modified from (Tomasini *et al*., 2008)
		R 5´-GTGCTGCTCAGCAGATTGAAC-3′	
CTGF	Human	F 5´-ACCGACTGGAAGACACGTTTG-3´	(Moreno-Vicente *et al*., 2018)
		´R 5´-CCAGGTCAGCTTCGCAAGG-3´	
CYR61	Human	F 5´-AGCCTCGCATCCTATACAACC-3´	(Cao and Zhao, 2019)
		R 5´-TTCTTTCACAAGGCGGCACTC-3´	
ANKRD1	Human	F 5´-AGTAGAGGAACTGGTCACTGG-3´	(Moreno-Vicente *et al*., 2018)
		R 5´-TGTTTCTCGCTTTTCCACTGTT-3´	

References

AASE, K., ERNKVIST, M., EBARASI, L., JAKOBSSON, L., MAJUMDAR, A., YI, C., BIROT, O., MING, Y., KVANTA, A., EDHOLM, D., ASPENSTRÖM, P., KISSIL, J., CLAESSON-WELSH, L., SHIMONO, A. & HOLMGREN, L. 2007. Angiomotin regulates endothelial cell migration during embryonic angiogenesis. *Genes & development,* 21**,** 2055-2068.

ABU TAHA, A. & SCHNITTLER, H.-J. 2014. Dynamics between actin and the VE-cadherin/catenin complex. *Cell Adhesion & Migration,* 8**,** 125-135.

AGOSTINI, M., ANNICCHIARICO-PETRUZZELLI, M., MELINO, G. & RUFINI, A. 2016. Metabolic pathways regulated by TAp73 in response to oxidative stress. *Oncotarget; Vol 7, No 21*.

AMELIO, I., INOUE, S., MARKERT, E. K., LEVINE, A. J., KNIGHT, R. A., MAK, T. W. & MELINO, G. 2015. TAp73 opposes tumor angiogenesis by promoting hypoxia-inducible factor 1α degradation. *Proceedings of the National Academy of Sciences,* 112**,** 226.

ANDERS, S. & HUBER, W. 2010. Differential expression analysis for sequence count data. *Genome Biology,* 11**,** R106.

ANDERS, S., PYL, P. T. & HUBER, W. 2015. HTSeq—a Python framework to work with high-throughput sequencing data. *Bioinformatics,* 31**,** 166-169.

ARANDA, J. F., REGLERO-REAL, N., MARCOS-RAMIRO, B., RUIZ-SÁENZ, A., FERNÁNDEZ-MARTÍN, L., BERNABÉ-RUBIO, M., KREMER, L., RIDLEY, A. J., CORREAS, I., ALONSO, M. A. & MILLÁN, J. 2012. MYADM controls endothelial barrier function through ERM-dependent regulation of ICAM-1 expression. *Molecular Biology of the Cell,* 24**,** 483-494.

AU - DAVIS, J., AU - CRAMPTON, S. P. & AU - HUGHES, C. C. W. 2007. Isolation of Human Umbilical Vein Endothelial Cells (HUVEC). *JoVE***,** e183.

BÁLINT, É., PHILLIPS, A. C., KOZLOV, S., STEWART, C. L. & VOUSDEN, K. H. 2002. Induction of p57^{KIP2} expression by p73β. *Proceedings of the National Academy of Sciences,* 99**,** 3529.

BENTLEY, K., FRANCO, C. A., PHILIPPIDES, A., BLANCO, R., DIERKES, M., GEBALA, V., STANCHI, F., JONES, M., ASPALTER, I. M., CAGNA, G., WESTRÖM, S., CLAESSON-WELSH, L., VESTWEBER, D. & GERHARDT, H. 2014. The role of differential VE-cadherin dynamics in cell rearrangement during angiogenesis. *Nature Cell Biology,* 16**,** 309-321.

BRATT, A., BIROT, O., SINHA, I., VEITONMÄKI, N., AASE, K., ERNKVIST, M. & HOLMGREN, L. 2005. Angiomotin Regulates Endothelial Cell-Cell Junctions and Cell Motility. *Journal of Biological Chemistry,* 280**,** 34859-34869.

BRESLIN, J. W., ZHANG, X. E., WORTHYLAKE, R. A. & SOUZA-SMITH, F. M. 2015. Involvement of Local Lamellipodia in Endothelial Barrier Function. *PLOS ONE,* 10**,** e0117970.

CAI, X., WANG, K.-C. & MENG, Z. 2021. Mechanoregulation of YAP and TAZ in Cellular Homeostasis and Disease Progression. *Frontiers in Cell and Developmental Biology,* 9.

CAO, J., EHLING, M., MÄRZ, S., SEEBACH, J., TARBASHEVICH, K., SIXTA, T., PITULESCU, M. E., WERNER, A.-C., FLACH, B., MONTANEZ, E., RAZ, E., ADAMS, R. H. & SCHNITTLER, H. 2017. Polarized actin and VE-cadherin dynamics regulate junctional remodelling and cell migration during sprouting angiogenesis. *Nature Communications,* 8**,** 2210.

CAO, J. & SCHNITTLER, H. 2019. Putting VE-cadherin into JAIL for junction remodeling. *Journal of Cell Science,* 132**,** jcs222893.

CAO, X. & ZHAO, B. 2019. Quantitative Real-Time PCR to Measure YAP/TAZ Activity in Human Cells. *In:* HERGOVICH, A. (ed.) *The Hippo Pathway: Methods and Protocols.* New York, NY: Springer New York.

CHÈNEBY, J., MÉNÉTRIER, Z., MESTDAGH, M., ROSNET, T., DOUIDA, A., RHALLOUSSI, W., BERGON, A., LOPEZ, F. & BALLESTER, B. 2020. ReMap 2020: a database of regulatory

regions from an integrative analysis of Human and Arabidopsis DNA-binding sequencing experiments. *Nucleic Acids Research,* 48**,** D180-D188.

CHOI, H.-J., ZHANG, H., PARK, H., CHOI, K.-S., LEE, H.-W., AGRAWAL, V., KIM, Y.-M. & KWON, Y.-G. 2015. Yes-associated protein regulates endothelial cell contact-mediated expression of angiopoietin-2. *Nature Communications,* 6**,** 6943.

CHUNG, H., LEE, B.-K., UPRETY, N., SHEN, W., LEE, J. & KIM, J. 2016. Yap1 is dispensable for self-renewal but required for proper differentiation of mouse embryonic stem (ES) cells. *EMBO reports,* 17**,** 519-529.

CLAESSON-WELSH, L. 2015. Vascular permeability--the essentials. *Upsala journal of medical sciences,* 120**,** 135-143.

CLAESSON-WELSH, L., DEJANA, E. & MCDONALD, D. M. 2021. Permeability of the Endothelial Barrier: Identifying and Reconciling Controversies. *Trends in Molecular Medicine,* 27**,** 314-331.

COLÁS-ALGORA, N., GARCÍA-WEBER, D., CACHO-NAVAS, C., BARROSO, S., CABALLERO, A., RIBAS, C., CORREAS, I. & MILLÁN, J. 2020. Compensatory increase of VE-cadherin expression through ETS1 regulates endothelial barrier function in response to TNFα. *Cellular and Molecular Life Sciences,* 77**,** 2125-2140.

CONFORTI, F., SAYAN, A. E., SREEKUMAR, R. & SAYAN, B. S. 2012. Regulation of p73 activity by post-translational modifications. *Cell death & disease,* 3**,** e285-e285.

DEJANA, E., ORSENIGO, F. & LAMPUGNANI, M. G. 2008. The role of adherens junctions and VE-cadherin in the control of vascular permeability. *Journal of Cell Science,* 121**,** 2115-2122.

DULLOO, I., HOOI, P. B. & SABAPATHY, K. 2015a. Hypoxia-induced DNp73 stabilization regulates Vegf-A expression and tumor angiogenesis similar to TAp73. *Cell cycle (Georgetown, Tex.),* 14**,** 3533-3539.

DULLOO, I., PHANG, B. H., OTHMAN, R., TAN, S. Y., VIJAYARAGHAVAN, A., GOH, L. K., MARTIN-LOPEZ, M., MARQUES, M. M., LI, C. W., WANG, DE Y., MARÍN, MARIA C., XIAN, W., MCKEON, F. & SABAPATHY, K. 2015b. Hypoxia-inducible TAp73 supports tumorigenesis by regulating the angiogenic transcriptome. *Nature Cell Biology,* 17**,** 511-523.

DURAN, C. L., HOWELL, D. W., DAVE, J. M., SMITH, R. L., TORRIE, M. E., ESSNER, J. J. & BAYLESS, K. J. 2017. Molecular Regulation of Sprouting Angiogenesis. *Comprehensive Physiology***,** 153-235.

ERNKVIST, M., PERSSON, N. L., AUDEBERT, S., LECINE, P., SINHA, I., LIU, M., SCHLUETER, M., HOROWITZ, A., AASE, K., WEIDE, T., BORG, J.-P., MAJUMDAR, A. & HOLMGREN, L. 2009. The Amot/Patj/Syx signaling complex spatially controls RhoA GTPase activity in migrating endothelial cells. *Blood,* 113**,** 244-253.

FERNANDEZ-ALONSO, R., MARTIN-LOPEZ, M., GONZALEZ-CANO, L., GARCIA, S., CASTRILLO, F., DIEZ-PRIETO, I., FERNANDEZ-CORONA, A., LORENZO-MARCOS, M. E., LI, X., CLAESSON-WELSH, L., MARQUES, M. M. & MARIN, M. C. 2015. p73 is required for endothelial cell differentiation, migration and the formation of vascular networks regulating VEGF and TGFβ signaling. *Cell Death & Differentiation,* 22**,** 1287-1299.

FERNÁNDEZ-MARTÍN, L., MARCOS-RAMIRO, B., BIGARELLA, C. L., GRAUPERA, M., CAIN, R. J., REGLERO-REAL, N., JIMÉNEZ, A., CERNUDA-MOROLLÓN, E., CORREAS, I., COX, S., RIDLEY, A. J. & MILLÁN, J. 2012. Crosstalk Between Reticular Adherens Junctions and Platelet Endothelial Cell Adhesion Molecule-1 Regulates Endothelial Barrier Function. *Arteriosclerosis, Thrombosis, and Vascular Biology,* 32**,** e90-e102.

FOLKMAN, J. 1971. Tumor Angiogenesis: Therapeutic Implications. *New England Journal of Medicine,* 285**,** 1182-1186.

FONTEMAGGI, G., KELA, I., AMARIGLIO, N., RECHAVI, G., KRISHNAMURTHY, J., STRANO, S., SACCHI, A., GIVOL, D. & BLANDINO, G. 2002. Identification of Direct p73 Target

Genes Combining DNA Microarray and Chromatin Immunoprecipitation Analyses *. *Journal of Biological Chemistry,* 277**,** 43359-43368.

FRANCO, C. A., JONES, M. L., BERNABEU, M. O., GEUDENS, I., MATHIVET, T., ROSA, A., LOPES, F. M., LIMA, A. P., RAGAB, A., COLLINS, R. T., PHNG, L.-K., COVENEY, P. V. & GERHARDT, H. 2015. Dynamic Endothelial Cell Rearrangements Drive Developmental Vessel Regression. *PLOS Biology,* 13**,** e1002125.

FUERTES-ALVAREZ, S., MAESO-ALONSO, L., VILLOCH-FERNANDEZ, J., WILDUNG, M., MARTIN-LOPEZ, M., MARSHALL, C., VILLENA-CORTES, A. J., DIEZ-PRIETO, I., PIETENPOL, J. A., TISSIR, F., LIZÉ, M., MARQUES, M. M. & MARIN, M. C. 2018. p73 regulates ependymal planar cell polarity by modulating actin and microtubule cytoskeleton. *Cell death & disease,* 9**,** 1183-1183.

GIAEVER, I. & KEESE, C. R. 1991. Micromotion of mammalian cells measured electrically. *Proceedings of the National Academy of Sciences,* 88**,** 7896.

GIANNOTTA, M., TRANI, M. & DEJANA, E. 2013. VE-Cadherin and Endothelial Adherens Junctions: Active Guardians of Vascular Integrity. *Developmental Cell,* 26**,** 441-454.

GONZALEZ-CANO, L., HILLJE, A. L., FUERTES-ALVAREZ, S., MARQUES, M. M., BLANCH, A., IAN, R. W., IRWIN, M. S., SCHWAMBORN, J. C. & MARÍN, M. C. 2013. Regulatory feedback loop between TP73 and TRIM32. *Cell death & disease,* 4**,** e704-e704.

GRESPI, F. & MELINO, G. 2012. P73 and age-related diseases: is there any link with Parkinson Disease? *Aging,* 4**,** 923-931.

HAYER, A., SHAO, L., CHUNG, M., JOUBERT, L.-M., YANG, H. W., TSAI, F.-C., BISARIA, A., BETZIG, E. & MEYER, T. 2016. Engulfed cadherin fingers are polarized junctional structures between collectively migrating endothelial cells. *Nature Cell Biology,* 18**,** 1311-1323.

HE, H., WANG, C., DAI, Q., LI, F., BERGHOLZ, J., LI, Z., LI, Q. & XIAO, Z.-X. 2016. p53 and p73 Regulate Apoptosis but Not Cell-Cycle Progression in Mouse Embryonic Stem Cells upon DNA Damage and Differentiation. *Stem cell reports,* 7**,** 1087-1098.

HE, Z., AGOSTINI, M., LIU, H., MELINO, G. & SIMON, H.-U. 2015. p73 regulates basal and starvation-induced liver metabolism in vivo. *Oncotarget; Vol 6, No 32*.

HEINKE, J., PATTERSON, C. & MOSER, M. 2012. Life is a pattern: vascular assembly within the embryo. *Frontiers in bioscience (Elite edition),* 4**,** 2269-2288.

HOOGLUGT, A., VAN DER STOEL, M. M., BOON, R. A. & HUVENEERS, S. 2021. Endothelial YAP/TAZ Signaling in Angiogenesis and Tumor Vasculature. *Frontiers in oncology,* 10**,** 612802-612802.

HUANG, D. W., SHERMAN, B. T. & LEMPICKI, R. A. 2008. Bioinformatics enrichment tools: paths toward the comprehensive functional analysis of large gene lists. *Nucleic Acids Research,* 37**,** 1-13.

HUANG, D. W., SHERMAN, B. T. & LEMPICKI, R. A. 2009. Systematic and integrative analysis of large gene lists using DAVID bioinformatics resources. *Nature Protocols,* 4**,** 44-57.

HULSEN, T., DE VLIEG, J. & ALKEMA, W. 2008. BioVenn – a web application for the comparison and visualization of biological lists using area-proportional Venn diagrams. *BMC Genomics,* 9**,** 488.

IRWIN, M. S., KONDO, K., MARIN, M. C., CHENG, L. S., HAHN, W. C. & KAELIN, W. G., JR. 2003. Chemosensitivity linked to p73 function. *Cancer Cell,* 3**,** 403-410.

JAKOBSSON, L., KREUGER, J. & CLAESSON-WELSH, L. 2007. Building blood vessels--stem cell models in vascular biology. *The Journal of cell biology,* 177**,** 751-755.

KOEPPEL, M., VAN HEERINGEN, S. J., KRAMER, D., SMEENK, L., JANSSEN-MEGENS, E., HARTMANN, M., STUNNENBERG, H. G. & LOHRUM, M. 2011. Crosstalk between c-Jun and TAp73α/β contributes to the apoptosis–survival balance. *Nucleic Acids Research,* 39**,** 6069-6085.

KOMAROVA, Y. A., KRUSE, K., MEHTA, D. & MALIK, A. B. 2017. Protein Interactions at Endothelial Junctions and Signaling Mechanisms Regulating Endothelial Permeability. *Circulation research,* 120**,** 179-206.

LANDRÉ, V., ANTONOV, A., KNIGHT, R. & MELINO, G. 2016. p73 promotes glioblastoma cell invasion by directly activating POSTN (periostin) expression. *Oncotarget,* 7**,** 11785-11802.

LENARD, A., ELLERTSDOTTIR, E., HERWIG, L., KRUDEWIG, A., SAUTEUR, L., BELTING, H.-G. & AFFOLTER, M. 2013. In Vivo Analysis Reveals a Highly Stereotypic Morphogenetic Pathway of Vascular Anastomosis. *Developmental Cell,* 25**,** 492-506.

LI, X. & CLAESSON-WELSH, L. 2009. Embryonic stem cell models in vascular biology. *Journal of Thrombosis and Haemostasis,* 7**,** 53-56.

LIVAK, K. J. & SCHMITTGEN, T. D. 2001. Analysis of relative gene expression data using real-time quantitative PCR and the 2(-Delta Delta C(T)) Method. *Methods,* 25**,** 402-8.

LIZAMA, C. O. & ZOVEIN, A. C. 2013. Polarizing pathways: Balancing endothelial polarity, permeability, and lumen formation. *Experimental Cell Research,* 319**,** 1247-1254.

LÓPEZ-FERRERAS, L., MARTÍNEZ-GARCÍA, N., MAESO-ALONSO, L., MARTÍN-LÓPEZ, M., DÍEZ-MATILLA, Á., VILLOCH-FERNANDEZ, J., ALONSO-OLIVARES, H., MARQUES, M. M. & MARIN, M. C. 2021. Deciphering the Nature of Trp73 Isoforms in Mouse Embryonic Stem Cell Models: Generation of Isoform-Specific Deficient Cell Lines Using the CRISPR/Cas9 Gene Editing System. *Cancers,* 13.

MAESO-ALONSO, L., LÓPEZ-FERRERAS, L., MARQUES, M. M. & MARIN, M. C. 2021. p73 as a Tissue Architect. *Frontiers in Cell and Developmental Biology,* 9.

MARCOS-RAMIRO, B., GARCÍA-WEBER, D., BARROSO, S., FEITO, J., ORTEGA, M. C., CERNUDA-MOROLLÓN, E., REGLERO-REAL, N., FERNÁNDEZ-MARTÍN, L., DURÁN, M. C., ALONSO, M. A., CORREAS, I., COX, S., RIDLEY, A. J. & MILLÁN, J. 2016. RhoB controls endothelial barrier recovery by inhibiting Rac1 trafficking to the cell border. *Journal of Cell Biology,* 213**,** 385-402.

MARTIN-LOPEZ, M., MAESO-ALONSO, L., FUERTES-ALVAREZ, S., BALBOA, D., RODRÍGUEZ-CORTEZ, V., WELTNER, J., DIEZ-PRIETO, I., DAVIS, A., WU, Y., OTONKOSKI, T., FLORES, E. R., MENÉNDEZ, P., MARQUES, M. M. & MARIN, M. C. 2017. p73 is required for appropriate BMP-induced mesenchymal-to-epithelial transition during somatic cell reprogramming. *Cell Death & Disease,* 8**,** e3034-e3034.

MATHELIER, A., FORNES, O., ARENILLAS, D. J., CHEN, C.-Y., DENAY, G., LEE, J., SHI, W., SHYR, C., TAN, G., WORSLEY-HUNT, R., ZHANG, A. W., PARCY, F., LENHARD, B., SANDELIN, A. & WASSERMAN, W. W. 2016. JASPAR 2016: a major expansion and update of the open-access database of transcription factor binding profiles. *Nucleic Acids Research,* 44**,** D110-D115.

MELINO, G., BERNASSOLA, F., RANALLI, M., YEE, K., ZONG, W. X., CORAZZARI, M., KNIGHT, R. A., GREEN, D. R., THOMPSON, C. & VOUSDEN, K. H. 2004. p73 Induces Apoptosis via PUMA Transactivation and Bax Mitochondrial Translocation. *Journal of Biological Chemistry,* 279**,** 8076-8083.

MORENO-VICENTE, R., PAVÓN, D. M., MARTÍN-PADURA, I., CATALÀ-MONTORO, M., DÍEZ-SÁNCHEZ, A., QUÍLEZ-ÁLVAREZ, A., LÓPEZ, J. A., SÁNCHEZ-ÁLVAREZ, M., VÁZQUEZ, J., STRIPPOLI, R. & DEL POZO, M. A. 2018. Caveolin-1 Modulates Mechanotransduction Responses to Substrate Stiffness through Actin-Dependent Control of YAP. *Cell Reports,* 25**,** 1622-1635.e6.

NAGY, J. A., DVORAK, A. M. & DVORAK, H. F. 2012. Vascular Hyperpermeability, Angiogenesis, and Stroma Generation. *Cold Spring Harbor Perspectives in Medicine,* 2.

NAPOLI, M. & FLORES, E. R. 2017. Another case for diet restriction: TAp73-expressing medulloblastomas are stunted by glutamine withdrawal. *Genes & development,* 31**,** 1715-1716.

NEMAJEROVA, A. & MOLL, U. M. 2019. Tissue-specific roles of p73 in development and homeostasis. *Journal of Cell Science,* 132**,** jcs233338.

NETO, F., KLAUS-BERGMANN, A., ONG, Y. T., ALT, S., VION, A.-C., SZYMBORSKA, A., CARVALHO, J. R., HOLLFINGER, I., BARTELS-KLEIN, E., FRANCO, C. A., POTENTE, M. & GERHARDT, H. 2018. YAP and TAZ regulate adherens junction dynamics and endothelial cell distribution during vascular development. *eLife,* 7**,** e31037.

NISHIOKA, N., INOUE, K.-I., ADACHI, K., KIYONARI, H., OTA, M., RALSTON, A., YABUTA, N., HIRAHARA, S., STEPHENSON, R. O., OGONUKI, N., MAKITA, R., KURIHARA, H., MORIN-KENSICKI, E. M., NOJIMA, H., ROSSANT, J., NAKAO, K., NIWA, H. & SASAKI, H. 2009. The Hippo Signaling Pathway Components Lats and Yap Pattern Tead4 Activity to Distinguish Mouse Trophectoderm from Inner Cell Mass. *Developmental Cell,* 16**,** 398-410.

OHASHI, T., IDOGAWA, M., SASAKI, Y. & TOKINO, T. 2017. p53 mediates the suppression of cancer cell invasion by inducing LIMA1/EPLIN. *Cancer Letters,* 390**,** 58-66.

PAGLIARI, S., VINARSKY, V., MARTINO, F., PERESTRELO, A. R., OLIVER DE LA CRUZ, J., CALUORI, G., VRBSKY, J., MOZETIC, P., POMPEIANO, A., ZANCLA, A., RANJANI, S. G., SKLADAL, P., KYTYR, D., ZDRÁHAL, Z., GRASSI, G., SAMPAOLESI, M., RAINER, A. & FORTE, G. 2021. YAP–TEAD1 control of cytoskeleton dynamics and intracellular tension guides human pluripotent stem cell mesoderm specification. *Cell Death & Differentiation,* 28**,** 1193-1207.

PIETSCH, E. C., SYKES, S. M., MCMAHON, S. B. & MURPHY, M. E. 2008. The p53 family and programmed cell death. *Oncogene,* 27**,** 6507-6521.

ROCA, C. & ADAMS, R. H. 2007. Regulation of vascular morphogenesis by Notch signaling. *Genes & Development,* 21**,** 2511-2524.

ROSE, A. B. 2019. Introns as Gene Regulators: A Brick on the Accelerator. *Frontiers in genetics,* 9**,** 672-672.

SABAPATHY, K. 2015. p73: a Positive or Negative Regulator of Angiogenesis, or Both? *Molecular and cellular biology,* 36**,** 848-854.

SANTOS GUASCH, G. L., BEELER, J. S., MARSHALL, C. B., SHAVER, T. M., SHENG, Q., JOHNSON, K. N., BOYD, K. L., VENTERS, B. J., COOK, R. S. & PIETENPOL, J. A. 2018. p73 Is Required for Ovarian Follicle Development and Regulates a Gene Network Involved in Cell-to-Cell Adhesion. *iScience,* 8**,** 236-249.

SAUTEUR, L., KRUDEWIG, A., HERWIG, L., EHRENFEUCHTER, N., LENARD, A., AFFOLTER, M. & BELTING, H.-G. 2014. Cdh5/VE-cadherin Promotes Endothelial Cell Interface Elongation via Cortical Actin Polymerization during Angiogenic Sprouting. *Cell Reports,* 9**,** 504-513.

SCHINDELIN, J., ARGANDA-CARRERAS, I., FRISE, E., KAYNIG, V., LONGAIR, M., PIETZSCH, T., PREIBISCH, S., RUEDEN, C., SAALFELD, S., SCHMID, B., TINEVEZ, J.-Y., WHITE, D. J., HARTENSTEIN, V., ELICEIRI, K., TOMANCAK, P. & CARDONA, A. 2012. Fiji: an open-source platform for biological-image analysis. *Nature Methods,* 9**,** 676-682.

SCHNEIDER, C. A., RASBAND, W. S. & ELICEIRI, K. W. 2012. NIH Image to ImageJ: 25 years of image analysis. *Nature Methods,* 9**,** 671-675.

SHANNON, P., MARKIEL, A., OZIER, O., BALIGA, N. S., WANG, J. T., RAMAGE, D., AMIN, N., SCHWIKOWSKI, B. & IDEKER, T. 2003. Cytoscape: a software environment for integrated models of biomolecular interaction networks. *Genome research,* 13**,** 2498-2504.

STANTIC, M., SAKIL, H. A. M., ZIRATH, H., FANG, T., SANZ, G., FERNANDEZ-WOODBRIDGE, A., MARIN, A., SUSANTO, E., MAK, T. W., ARSENIAN HENRIKSSON, M. & WILHELM, M. T. 2015. TAp73 suppresses tumor angiogenesis through repression of proangiogenic cytokines and HIF-1α activity. *Proceedings of the National Academy of Sciences,* 112**,** 220.

STRANO, S., MONTI, O., PEDICONI, N., BACCARINI, A., FONTEMAGGI, G., LAPI, E., MANTOVANI, F., DAMALAS, A., CITRO, G., SACCHI, A., DEL SAL, G., LEVRERO, M.

& BLANDINO, G. 2005. The Transcriptional Coactivator Yes-Associated Protein Drives p73 Gene-Target Specificity in Response to DNA Damage. *Molecular Cell,* 18**,** 447-459.

SZYMBORSKA, A. & GERHARDT, H. 2018. Hold Me, but Not Too Tight—Endothelial Cell–Cell Junctions in Angiogenesis. *Cold Spring Harbor Perspectives in Biology,* 10.

TIRUPPATHI, C., MALIK, A. B., DEL VECCHIO, P. J., KEESE, C. R. & GIAEVER, I. 1992. Electrical method for detection of endothelial cell shape change in real time: assessment of endothelial barrier function. *Proceedings of the National Academy of Sciences of the United States of America,* 89**,** 7919-7923.

TISSIR, F., RAVNI, A., ACHOURI, Y., RIETHMACHER, D., MEYER, G. & GOFFINET, A. M. 2009. DeltaNp73 regulates neuronal survival in vivo. *Proceedings of the National Academy of Sciences,* 106**,** 16871.

TOMASINI, R., TSUCHIHARA, K., WILHELM, M., FUJITANI, M., RUFINI, A., CHEUNG, C. C., KHAN, F., ITIE-YOUTEN, A., WAKEHAM, A., TSAO, M.-S., IOVANNA, J. L., SQUIRE, J., JURISICA, I., KAPLAN, D., MELINO, G., JURISICOVA, A. & MAK, T. W. 2008. TAp73 knockout shows genomic instability with infertility and tumor suppressor functions. *Genes & development,* 22**,** 2677-2691.

TSOGTBAATAR, E., LANDIN, C., MINTER-DYKHOUSE, K. & FOLMES, C. D. L. 2020. Energy Metabolism Regulates Stem Cell Pluripotency. *Frontiers in Cell and Developmental Biology,* 8.

UEMURA, A., KUSUHARA, S., KATSUTA, H. & NISHIKAWA, S.-I. 2006. Angiogenesis in the mouse retina: A model system for experimental manipulation. *Experimental Cell Research,* 312**,** 676-683.

VIKHREVA, P., MELINO, G. & AMELIO, I. 2018. p73 Alternative Splicing: Exploring a Biological Role for the C-Terminal Isoforms. *Journal of Molecular Biology,* 430**,** 1829-1838.

WANG, W., LI, N., LI, X., TRAN, M. K., HAN, X. & CHEN, J. 2015. Tankyrase Inhibitors Target YAP by Stabilizing Angiomotin Family Proteins. *Cell reports,* 13**,** 524-532.

WANG, X. Q., ONGKEKO, W. M., LAU, A. W. S., LEUNG, K. M. & POON, R. Y. C. 2001. A Possible Role of p73 on the Modulation of p53 Level through MDM2. *Cancer Research,* 61**,** 1598.

WEI, C.-L., WU, Q., VEGA, V. B., CHIU, K. P., NG, P., ZHANG, T., SHAHAB, A., YONG, H. C., FU, Y., WENG, Z., LIU, J., ZHAO, X. D., CHEW, J.-L., LEE, Y. L., KUZNETSOV, V. A., SUNG, W.-K., MILLER, L. D., LIM, B., LIU, E. T., YU, Q., NG, H.-H. & RUAN, Y. 2006. A Global Map of p53 Transcription-Factor Binding Sites in the Human Genome. *Cell,* 124**,** 207-219.

XIE, N., VIKHREVA, P., ANNICCHIARICO-PETRUZZELLI, M., AMELIO, I., BARLEV, N., KNIGHT, R. A. & MELINO, G. 2018. Integrin-β4 is a novel transcriptional target of TAp73. *Cell cycle (Georgetown, Tex.),* 17**,** 589-594.

YANG, A., WALKER, N., BRONSON, R., KAGHAD, M., OOSTERWEGEL, M., BONNIN, J., VAGNER, C., BONNET, H., DIKKES, P., SHARPE, A., MCKEON, F. & CAPUT, D. 2000. p73-deficient mice have neurological, pheromonal and inflammatory defects but lack spontaneous tumours. *Nature,* 404**,** 99-103.

ZALTSMAN, Y., MASUKO, S., BENSEN, J. J. & KIESSLING, L. L. 2019. Angiomotin Regulates YAP Localization during Neural Differentiation of Human Pluripotent Stem Cells. *Stem cell reports,* 12**,** 869-877.

ZENG, X., CHEN, L., JOST, C. A., MAYA, R., KELLER, D., WANG, X., KAELIN, W. G., OREN, M., CHEN, J. & LU, H. 1999. MDM2 Suppresses p73 Function without Promoting p73 Degradation. *Molecular and Cellular Biology,* 19**,** 3257.

ZHANG, Y., ZHANG, Y., KAMEISHI, S., BARUTELLO, G., ZHENG, Y., TOBIN, N. P., NICOSIA, J., HENNIG, K., CHIU, D. K.-C., BALLAND, M., BARKER, T. H., CAVALLO, F. & HOLMGREN, L. 2021. The Amot/integrin protein complex transmits mechanical forces required for vascular expansion. *Cell Reports,* 36**,** 109616.

ZHAO, B., LI, L., LU, Q., WANG, L. H., LIU, C.-Y., LEI, Q. & GUAN, K.-L. 2011. Angiomotin is a novel Hippo pathway component that inhibits YAP oncoprotein. *Genes & Development,* 25**,** 51-63.

ZHENG, Y., VERTUANI, S., NYSTRÖM, S., AUDEBERT, S., MEIJER, I., TEGNEBRATT, T., BORG, J.-P., UHLÉN, P., MAJUMDAR, A. & HOLMGREN, L. 2009. Angiomotin-Like Protein 1 Controls Endothelial Polarity and Junction Stability During Sprouting Angiogenesis. *Circulation Research,* 105**,** 260-270.

ZHU, J., JIANG, J., ZHOU, W. & CHEN, X. 1998. The Potential Tumor Suppressor p73 Differentially Regulates Cellular p53 Target Genes. *Cancer Research,* 58**,** 5061.

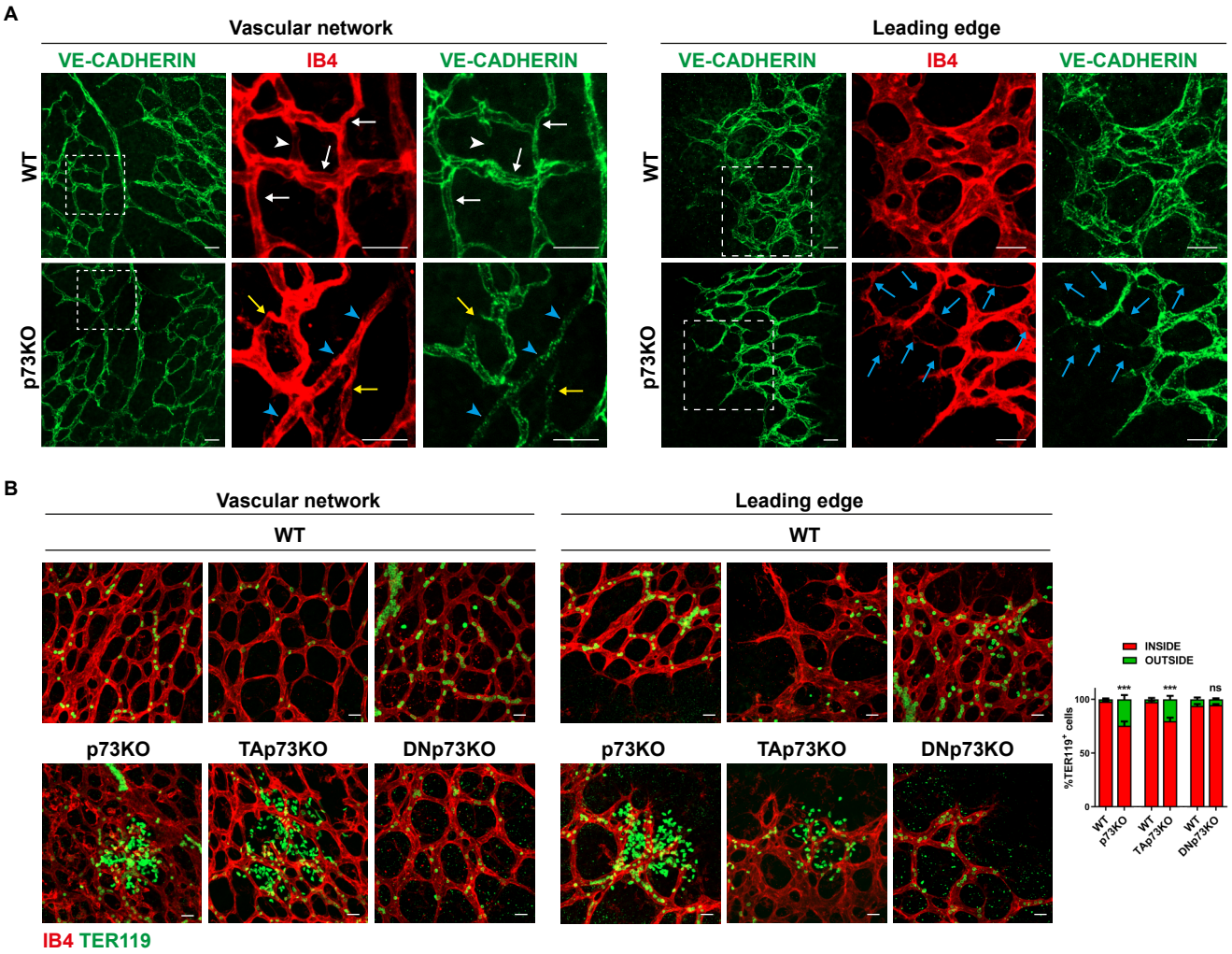

Maeso-Alonso et al. Figure 1

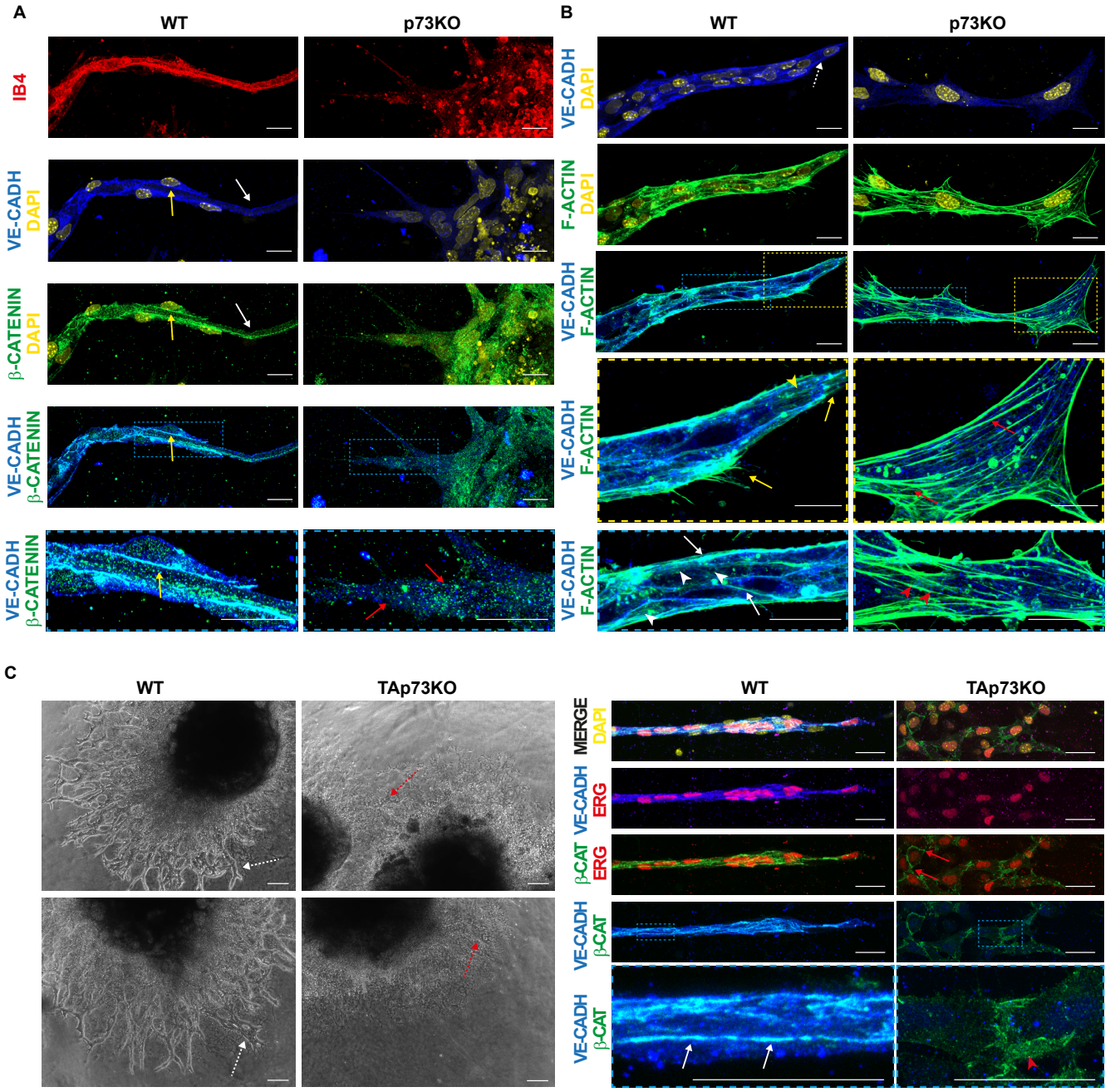

Maeso-Alonso et al. Figure 2

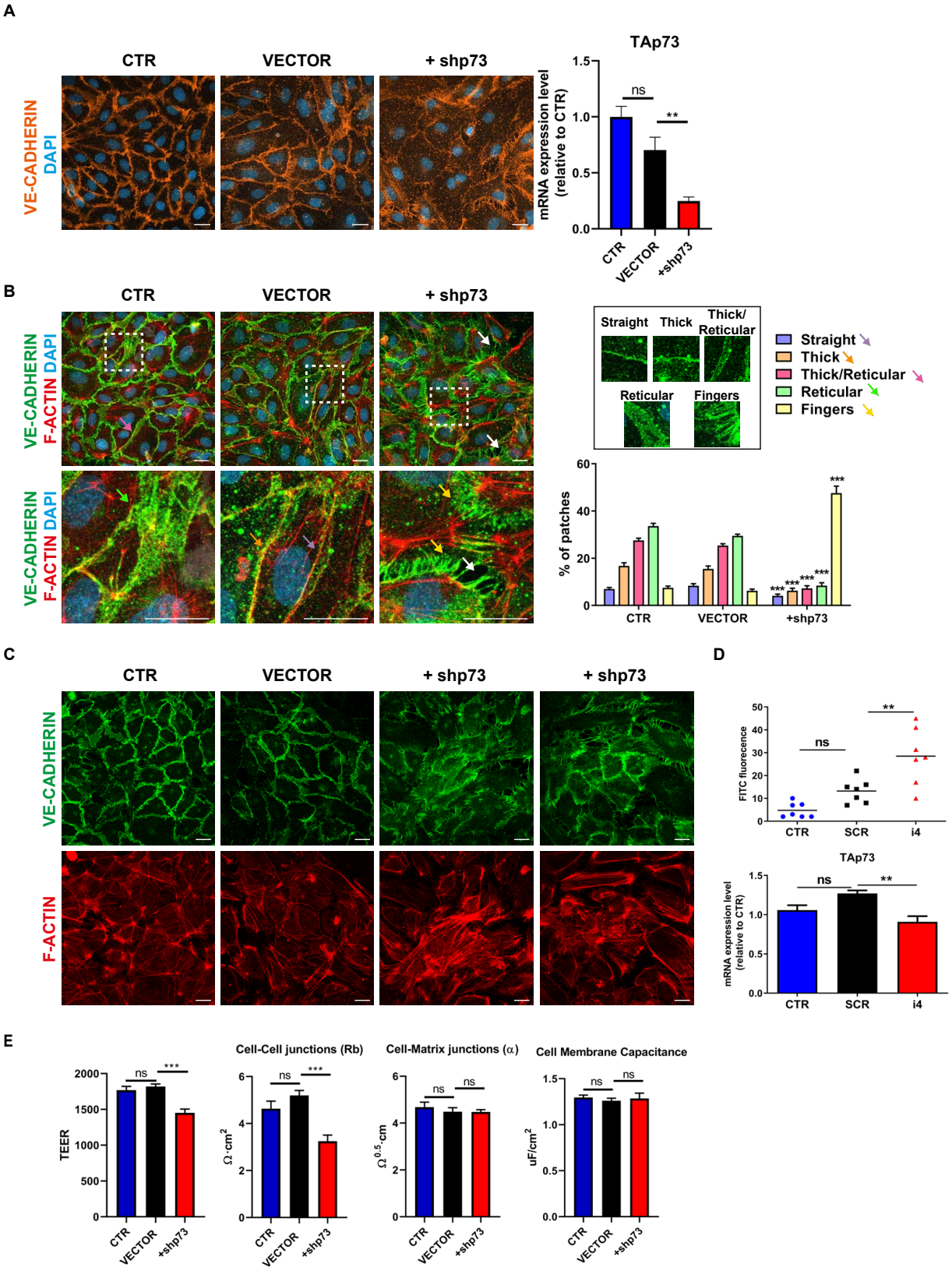

Maeso-Alonso et al. Figure 3

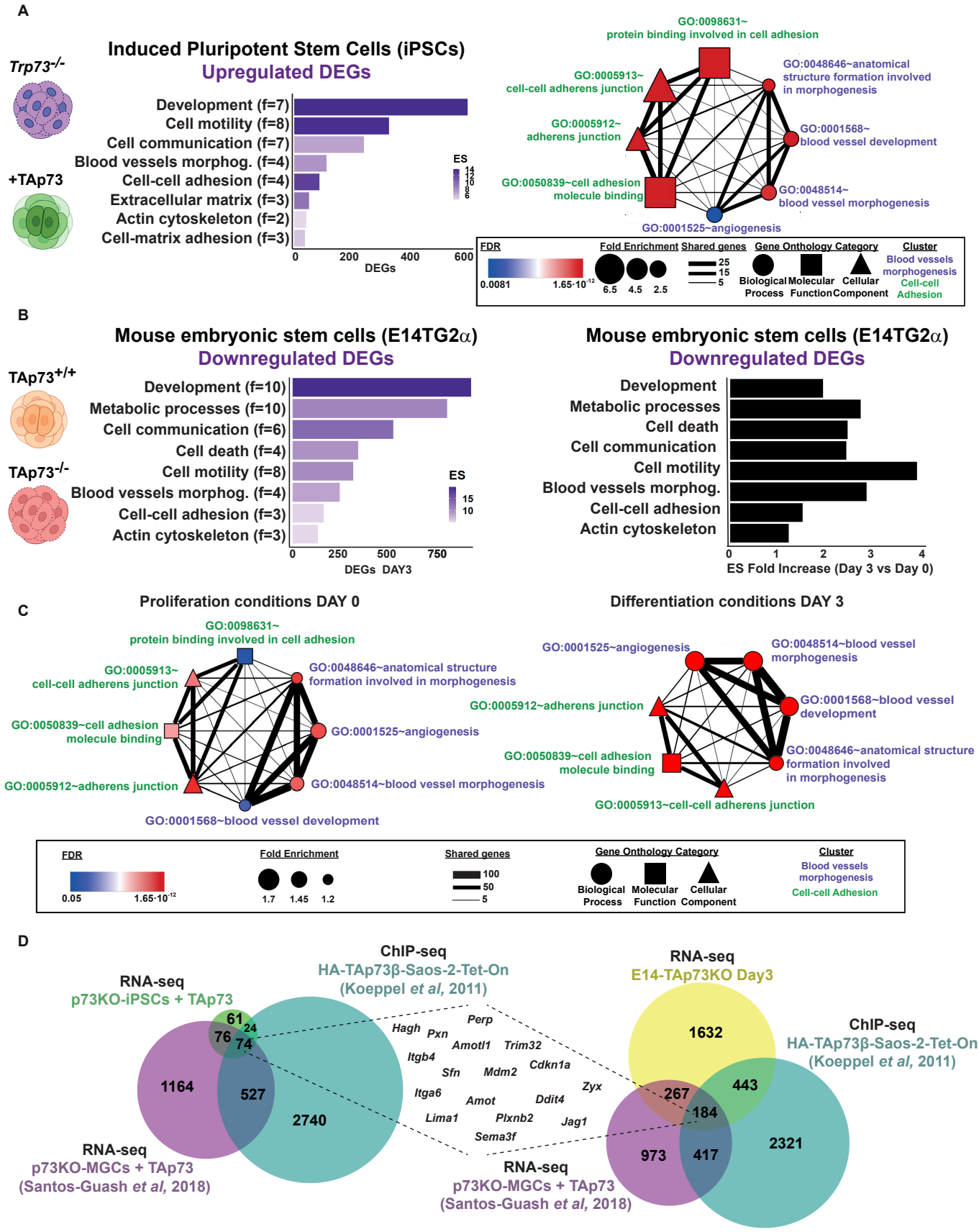

Maeso-Alonso et al. Figure 4

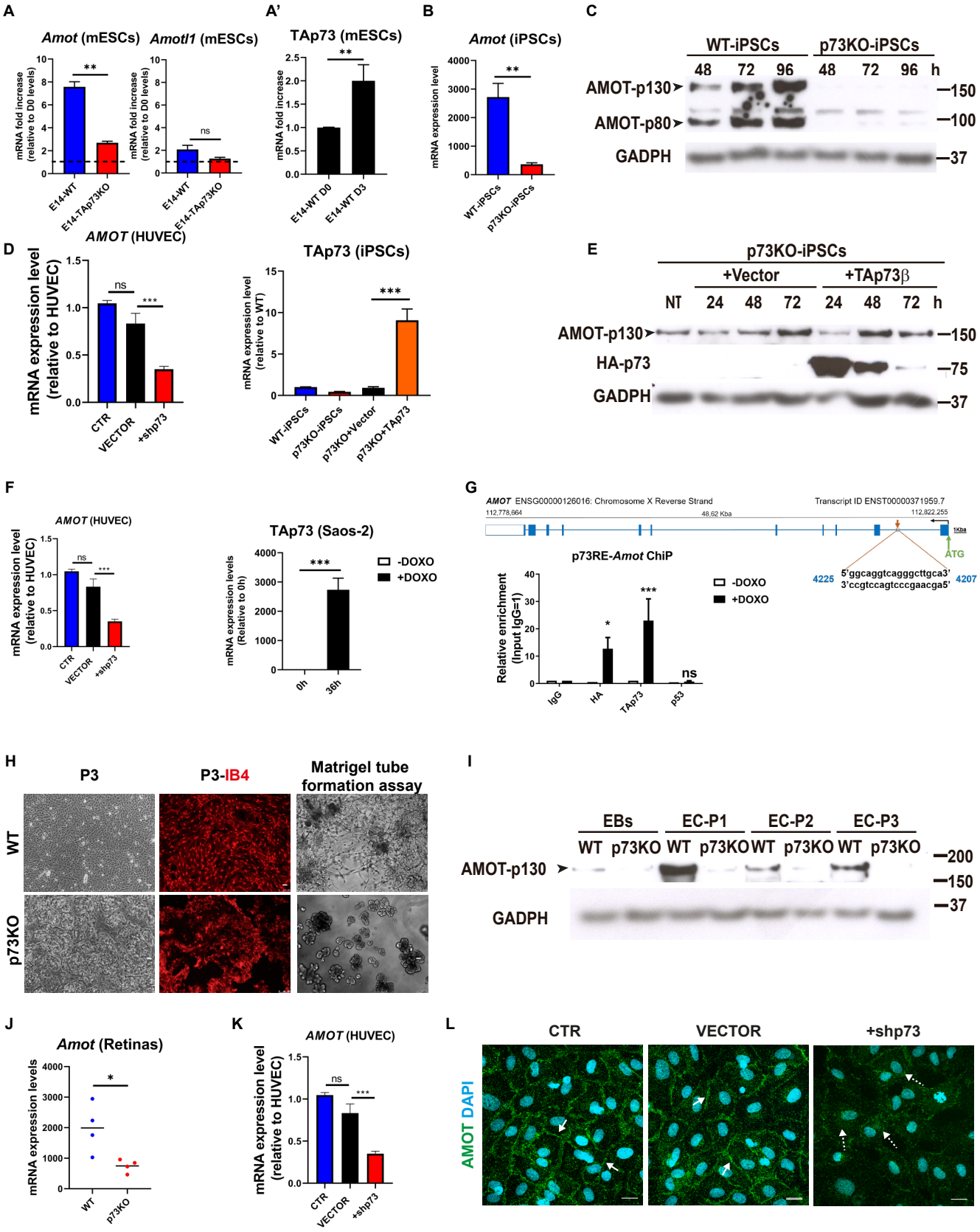

Maeso-Alonso et al. Figure 5

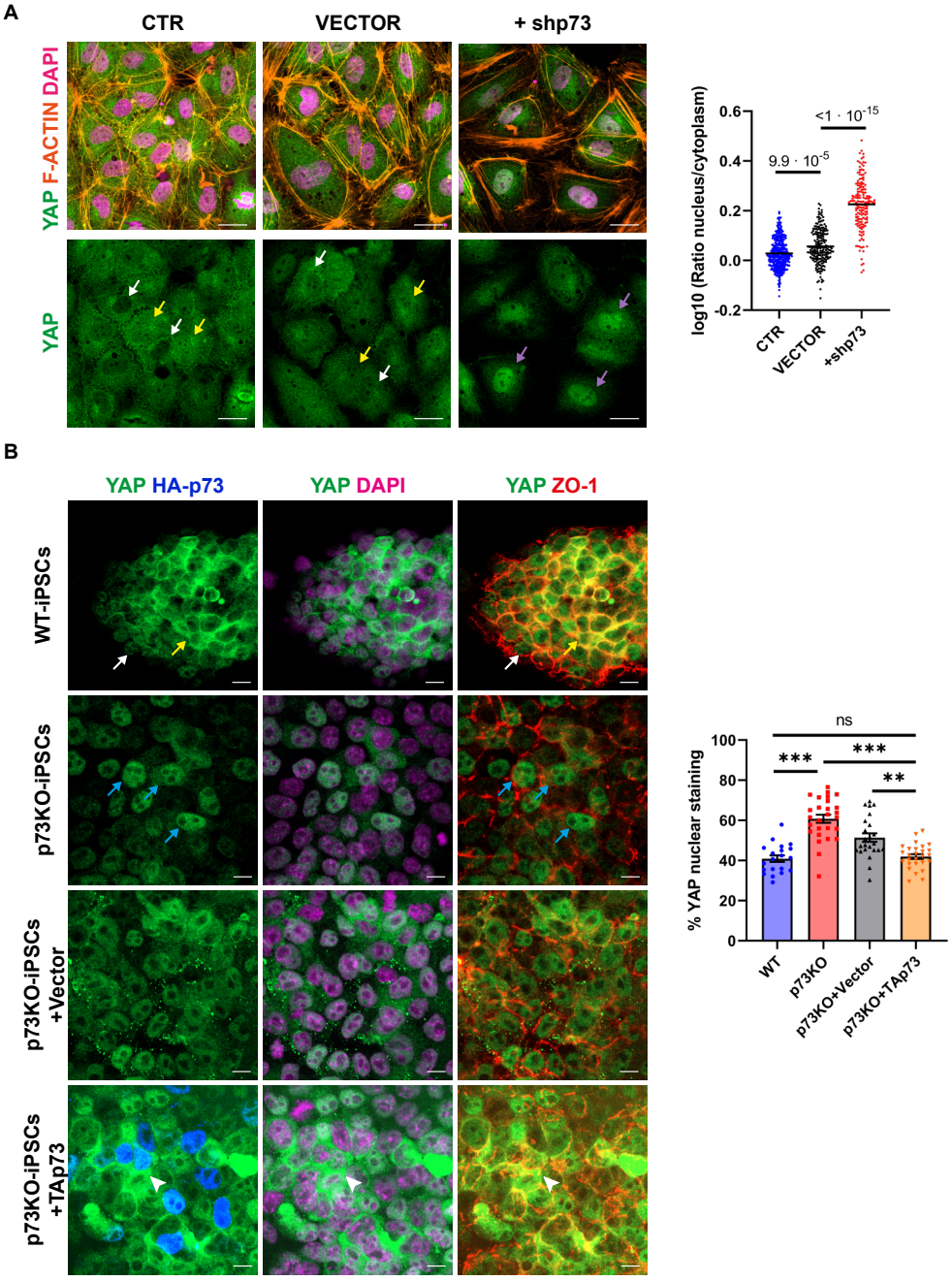

Maeso-Alonso et al. Figure 6

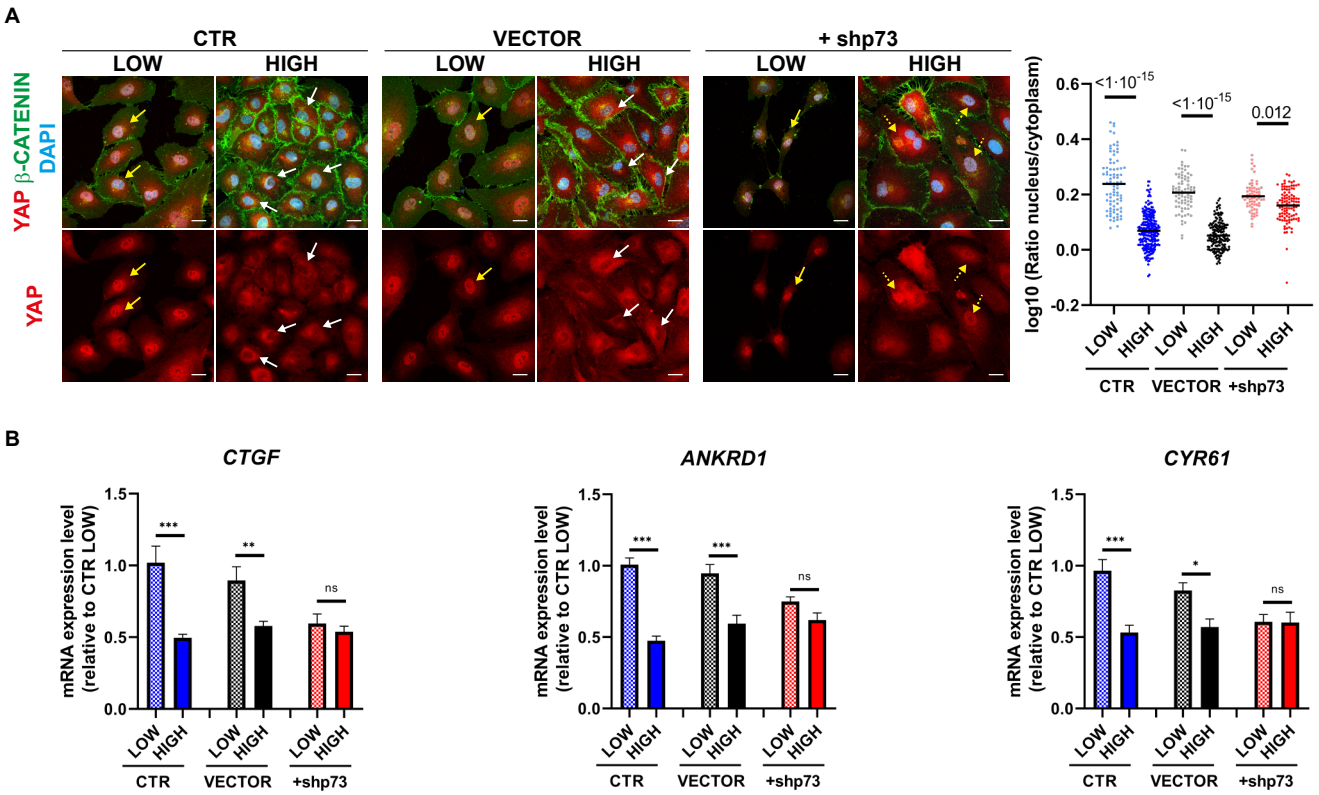

Maeso-Alonso et al. Figure 7

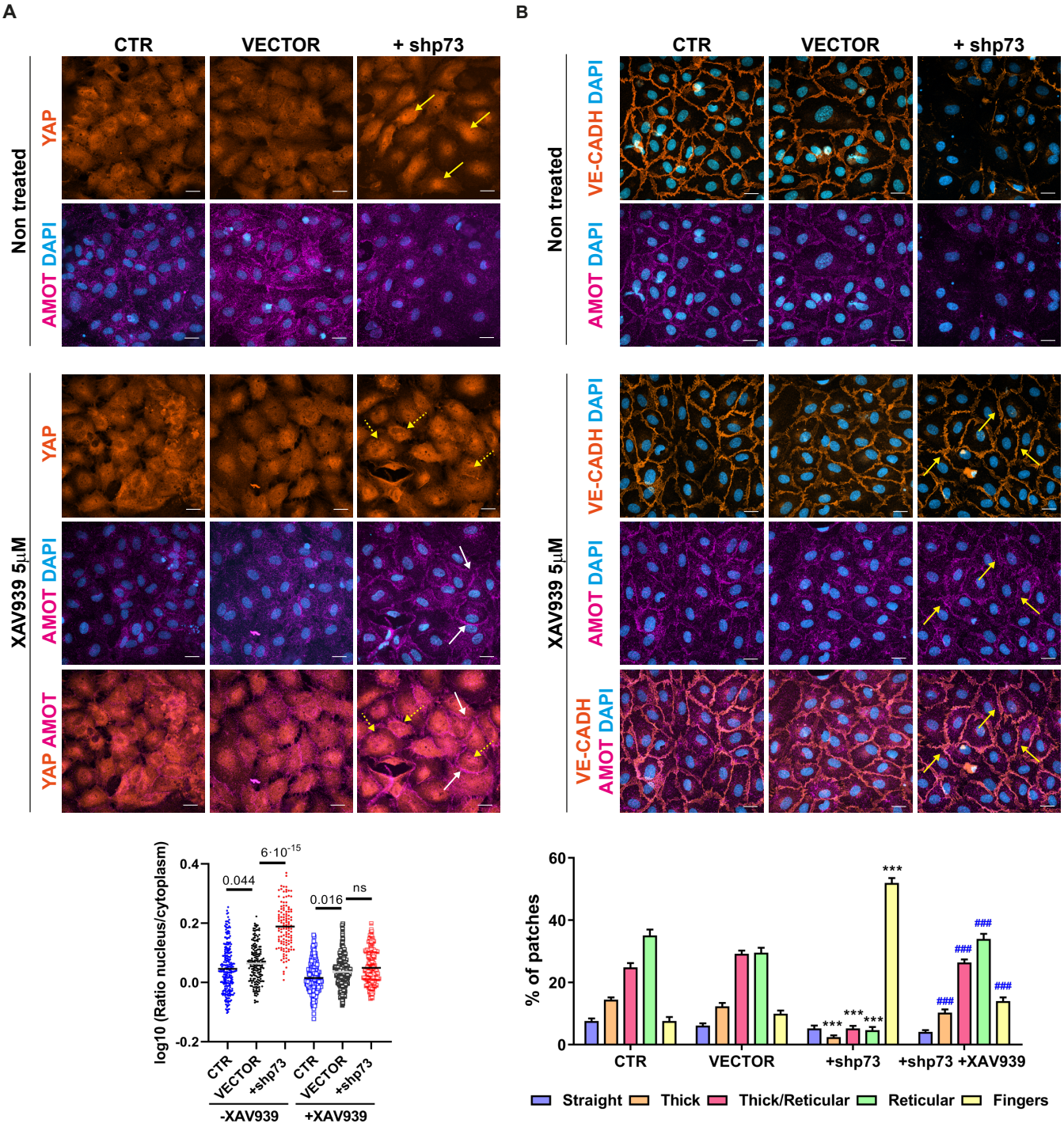

Maeso-Alonso et al. Figure 8

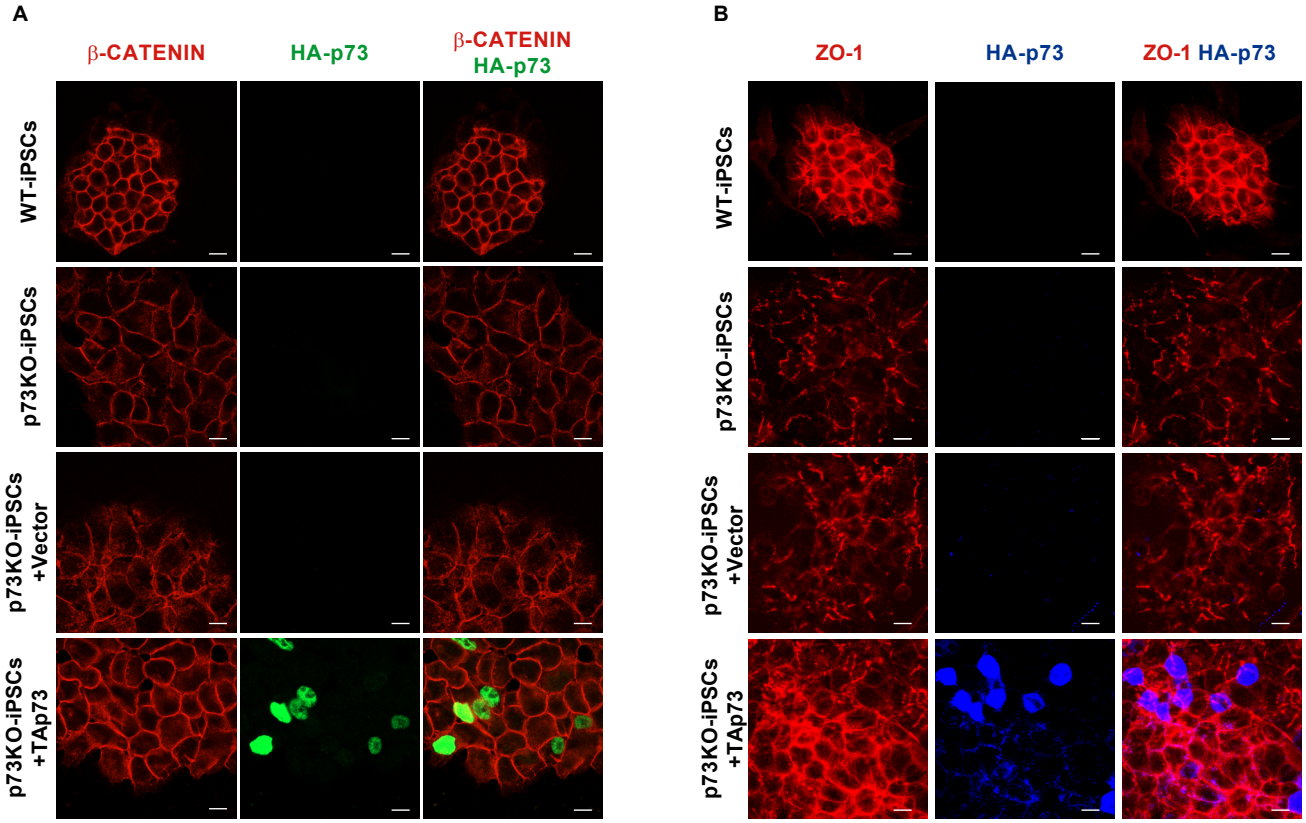

Maeso-Alonso et al. Supplementary Figure 1